



TECHNISCHE
UNIVERSITÄT
WIEN

DIPLOMARBEIT

Repair Solutions for PV Modules with Cracked Backsheets

zur Erlangung des akademischen Grades

Diplom-Ingenieur

im Rahmen des Studiums

Physikalische Energie- und Messtechnik

eingereicht von

Raffael Leo Schifferegger, BSc

Matrikelnummer: 01615508

ausgeführt am Institut für Angewandte Physik (IAP)
der Fakultät für Physik der Technischen Universität Wien
in Zusammenarbeit mit dem Österreichisches Forschungsinstitut für Chemie und Technik (OFI)

unter der Betreuung durch
Ao.Univ.-Prof. Dipl.-Ing. Dr. techn. Martin **Gröschl** (IAP)
Dipl.-Ing. Dr. techn. Gabriele C. **Eder** (OFI)

Wien, 29.01.2025

(Unterschrift Verfasser/in)

(Unterschrift Betreuer/in)

Abstract

The transition to clean, renewable energy sources is a pressing global priority, and photovoltaics (PV) stand at the forefront of this shift. With rapidly increasing installation rates, PV systems are expected to become a cornerstone of low-carbon power generation. However, while technological advancements have enhanced module efficiency, backsheet related issues can lead to a shortened lifespan of the module. Cracks in these backsheets can compromise electrical insulation, posing safety risks and potentially causing inverter shutdowns, which leads to performance losses.

This thesis investigates multiple backsheet repair methods—including two specialized coatings (one polyurethane-based and one silicone-based) and a PVC tape solution—applied to cracked modules. To evaluate the effectiveness of each approach, the repaired modules were subjected to an accelerated aging test comprising damp heat and temperature cycling to simulate challenging operational conditions. Crack-filling efficacy was assessed by light and ultrasonic microscopy and ATR-IR imaging, while infrared spectroscopy was used to monitor chemical changes and degradation on the surface. The silicone-based coating was the most durable, while the polyurethane-based coating and PVC tape exhibited cracking and failed the insulation resistance test. Only minor chemical changes were observed during aging. The PVC tape was unable to fill deep cracks, whereas both silicone and polyurethane coatings effectively filled them, as evidenced by ATR-IR and light microscopy. Electrical insulation and performance were analyzed through insulation resistance and I-V-measurements, respectively. Electroluminescence measurements revealed no significant differences in cell degradation across the repair methods.

Zusammenfassung

Der Übergang zu sauberen, erneuerbaren Energiequellen ist eine dringende globale Priorität, und die Photovoltaik (PV) steht an der Spitze dieses Wandels. Mit den rasant steigenden Installationsraten wird erwartet, dass PV-Systeme zu einer tragenden Säule der kohlenstoffarmen Energieerzeugung werden. Technologische Fortschritte haben zwar die Effizienz der Module verbessert, jedoch können Probleme mit der Rückseitenfolie die Lebensdauer der Module verkürzen. Risse in diesen Rückseitenfolien können die elektrische Isolierung beeinträchtigen, Sicherheitsrisiken darstellen und potenziell zu Wechselrichterabschaltungen führen, was wiederum Leistungsverluste zur Folge hat.

Diese Arbeit untersucht mehrere Methoden zur Reparatur von Rückseitenfolien, darunter zwei spezielle Beschichtungen (eine auf Polyurethanbasis und eine auf Silikonbasis) sowie eine Lösung mit PVC-Klebeband, die auf rissige Module angewendet wurden. Um die Wirksamkeit der einzelnen Ansätze zu bewerten, wurden die reparierten Module einem beschleunigten Alterungstest unterzogen, der aus Feuchte-Wärme- und Temperaturwechselzyklen bestand, um herausfordernde Betriebsbedingungen zu simulieren. Die Effektivität der Rissfüllung wurde mittels Licht- und Ultraschallmikroskopie sowie ATR-Infrarot-Bildgebung (ATR-IR) untersucht, während mit Infrarotspektroskopie chemische Veränderungen und Degradationen an der Oberfläche überwacht wurden. Die silikonbasierte Beschichtung erwies sich als am langlebigsten, während die Polyurethan-Beschichtung und das PVC-Klebeband Risse zeigten und den Isolationswiderstandstest nicht bestanden. Während des Alterungstests wurden nur geringe chemische Veränderungen beobachtet. Das PVC-Klebeband konnte tiefe Risse nicht füllen, während sowohl die Silikon- als auch die Polyurethan-Beschichtungen diese effektiv füllten, wie durch ATR-IR und Lichtmikroskopie nachgewiesen wurde. Die elektrische Isolierung und Leistung wurden durch Isolationswiderstands- und I-V-Messungen analysiert. Elektrolumineszenzmessungen zeigten keine signifikanten Unterschiede in der Zelldegradation zwischen den Reparaturmethoden.

Acknowledgements

I would like to express my heartfelt gratitude to my supervisors, Gabriele Eder and Anika Gassner, for granting me the invaluable opportunity to write my master's thesis at OFI and for introducing me to the fascinating field of photovoltaics. Their guidance, patience, and willingness to share their extensive knowledge have been essential in shaping my understanding of material analysis, spectroscopy, and photovoltaic technologies. I am deeply thankful for their support throughout this journey, not only in helping with material measurements and analysis but also in awakening my interest for research and the world of photovoltaics.

I would also like to extend my sincere thanks to my colleagues at OFI for their collaborative spirit and assistance during my experiments. I am especially grateful to Yuliya Voronko for her help which greatly contributed to the progress of my work.

Furthermore, I wish to acknowledge my supervisor at TU Wien, Professor Gröschl, for enabling this external thesis and providing administrative support.

Finally, I am grateful for the warm and supportive environment at OFI, which allowed me to grow both academically and personally, and for the opportunity to contribute to this meaningful area of research.

January 29, 2025

Raffael Leo Schifferegger

Contents

1	Introduction	9
1.1	Photovoltaic Module Design	10
1.2	Polymeric Backsheets	11
1.3	Typical Failure Modes in PV Modules	12
1.4	Polyamide Backsheet Failures	12
1.5	ReNew PV research project	13
1.6	Research Questions	13
2	Sample description	15
2.1	PV Modules with Polyamide Backsheets	15
2.2	PV Module Specifications and Origin	15
3	Characterization Methods	17
3.1	Visual Inspection and Microscopy	17
3.1.1	Visual Inspection	17
3.1.2	Light Microscopy	17
3.1.3	Ultrasonic Microscopy	18
3.2	Infrared Spectroscopy (IR)	20
3.2.1	IR Spectrometer	21
3.3	Electrical Characterization	22
3.3.1	Power Measurement	22
3.3.2	Electroluminescence Measurement	24
3.3.3	Insulation Resistance Measurements	24
4	Backsheet Repair: Methodology and long-term Stability	27
4.1	Repair Materials and their Application to the Backsheet	27
4.2	Crack Filling Analysis	28
4.2.1	Descriptions of the Coating Process	30
4.2.2	Non-Destructive Measurements: Scanning Acoustic Microscopy (SAM)	31
4.2.3	Destructive Measurements	34
4.3	Main Experiment: Backsheet Repair on aged Photovoltaic Modules	37
4.3.1	Silicone (DOWSil)	37
4.3.2	Polyurethane (Remisol)	38
4.3.3	Foil: PVC-Tape with acrylic adhesive (3M 1080)	40
4.3.4	Wet Leakage Test	40
4.4	Weathering through temperature cycles	41
4.4.1	Silicone Coating (M1)	44
4.4.2	PU Coating (M2, M3, M6, M7)	45
4.4.3	Tape (M4)	52
4.4.4	Uncoated Reference Module (M5)	53
4.5	IR Spectroscopy	54

4.6	Performance measurements	60
4.7	Electroluminescence measurements	60
4.8	Conclusion	61
5	Discussion	65
5.1	What is the most reliable method for examining the crack-filling effectiveness of repair coatings?	65
5.2	How do the applied coatings perform under accelerated aging conditions?	65
5.3	Which repair approach is most suitable for different types of cracks in PV backsheets?	66
5.4	Practical Implications	67
5.5	Critical Analysis	67
5.6	Limitations	67
6	Summary and Outlook	69
6.1	Summary	69
6.2	Outlook and Recommendations for Future Work	69
7	Bibliography	71
	List of Figures	79
	List of Tables	81

Chapter 1

Introduction

The global energy landscape is undergoing a significant transformation as nations strive to mitigate the impacts of climate change and transition to sustainable energy sources. Fossil fuels, which still dominate global energy production, are not only finite but also the primary contributors to greenhouse gas emissions. The pressing need to address the climate crisis has led to ambitious renewable energy targets worldwide. For instance, the European Union (EU) has committed to generating 45 % of its energy from renewable sources by 2030 as part of the REPowerEU plan, with photovoltaics (PV) expected to contribute 600 GW of this capacity [8]. In Austria, the transition to renewables mirrors this urgency. By 2030, Austria aims to produce 100 % of its electricity from renewable sources, with PV projected to account for a substantial share. Meeting this goal will require expanding PV electricity generation substantially even though Austria has reached a share of 10 % in 2023 [5]. The affordability of PV systems, now among the cheapest energy sources in the EU, further underscores their importance. This dual advantage – environmental sustainability and economic feasibility – positions PV as a cornerstone of the energy transition.

While PV modules offer a clean and renewable energy solution during operation, their sustainability across the entire lifecycle is a critical consideration. Manufacturing processes, although improving, still consume high amounts of energy and resources especially in the production plus a smaller amount for the End-of-Life phase. However, modern mono crystalline silicon modules in Europe can achieve a non renewable energy payback time of 1 year, depending on installation conditions and operational lifespans exceeding 25 years [33, 25, 14]. Despite this, end-of-life (EOL) management remains a significant challenge. With increasing deployments, the volume of PV waste will rise sharply in the coming decades, necessitating effective recycling and repair strategies to minimize environmental impact [13].

Addressing these module failures through effective repair strategies can significantly extend module lifetimes, reducing both waste generation and the need for premature replacements. In this context, repair of PV module backsheets – a common point of failure – offers a sustainable and economically viable solution. Backsheets, which protect the module's internal components from mechanical impact, environmental exposure and provide electrical insulation, are critical for maintaining performance and safety. Over time, environmental stressors such as UV radiation, temperature fluctuations, and mechanical loads can degrade the backsheet, leading to cracks, delamination, or other defects [12]. These failures not only reduce the module's efficiency but can also pose safety risks.

Repairing backsheets extends the functional life of PV modules, delaying their disposal and reducing the demand for new materials and energy-intensive manufacturing. This approach aligns with circular economy principles and can offer both environmental and economic benefits. By addressing common failure mechanisms and developing effective repair solutions, this research

contributes to enhancing the long-term sustainability of PV systems.

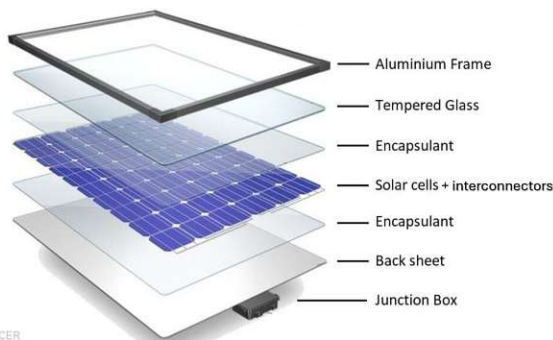
According to a comprehensive study by Jordan et al. [29], the median degradation rate for PV modules is approximately 0.5% to 0.6% per year, with variations depending on the module design, materials, and environmental conditions at the installation site. Over a typical operational lifespan of 25 years (which is the typical warranty time of PV panels), this equates to a performance loss of roughly 12.5%, although some modules degrade at rates as low as 0.1% per year, while others may experience rates exceeding 1%. Understanding these degradation trends is critical for predicting module performance and designing maintenance or repair strategies.

1.1 Photovoltaic Module Design

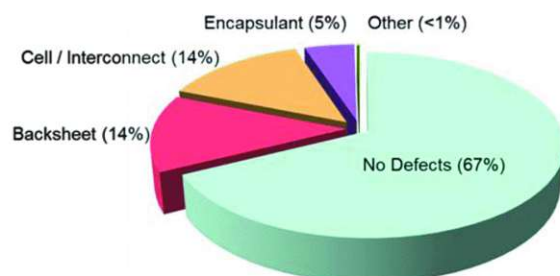
Understanding the construction/design of a PV module is essential for identifying potential failure points and developing effective repair solutions. As illustrated in Figure 1.1a, a typical glass/backsheet PV module consists of several layers, each playing a crucial role:

- **Front glass:** a durable, transparent layer that protects the polymeric and encapsulant and solar cells from environmental damage while allowing sunlight to pass through.
- **Encapsulant:** layers of polymer material that provide mechanical support and protection for the solar cells and the current-carrying metallic interconnectors.
- **Solar cells and interconnectors:** core components of the module, converting sunlight into electricity and transporting it.
- **Backsheet:** protective rear layer, often made of a polymer materials in a multi layered stack that shields the module’s internal components from external conditions and provides electrical insulation.
- **Frame and junction box:** The frame provides structural support, while the junction box facilitates electrical connections.

This layered multi-material structure ensures module reliability under various environmental conditions while maximizing energy conversion efficiency.



(a) Typical layer structure of a glass-backsheet module [49].



(b) Distribution of defects in PV modules, high-lighting backsheet failures [53].

Figure 1.1: Overview of PV module structure and defect distribution.

1.2 Polymeric Backsheets

The backsheet of a PV module serves multiple critical functions that contribute to the performance, longevity, and safety of the module. As the outermost layer on the rear side of the module, it provides mechanical protection against environmental stressors such as moisture, UV radiation, and physical impacts. The backsheet acts as an insulating barrier, preventing electrical hazards by isolating the internal conductive components of the module from external elements and protecting living beings from electric shocks. Furthermore, it supports the structural integrity of the module by providing dimensional stability and minimizing mechanical stress on the encapsulant and solar cells, especially during thermal cycling. High reflectivity of the inner surface of some backsheets (interlayer to encapsulant) also improves module efficiency by reflecting "unused" sunlight and therefore keeping the module temperature lower. Due to its protective and functional roles, the backsheet must maintain its performance over the module's lifespan, often exceeding 25 years, under a wide range of environmental conditions. This makes the selection of backsheet materials and construction critical to ensuring both reliability and sustainability in PV systems.

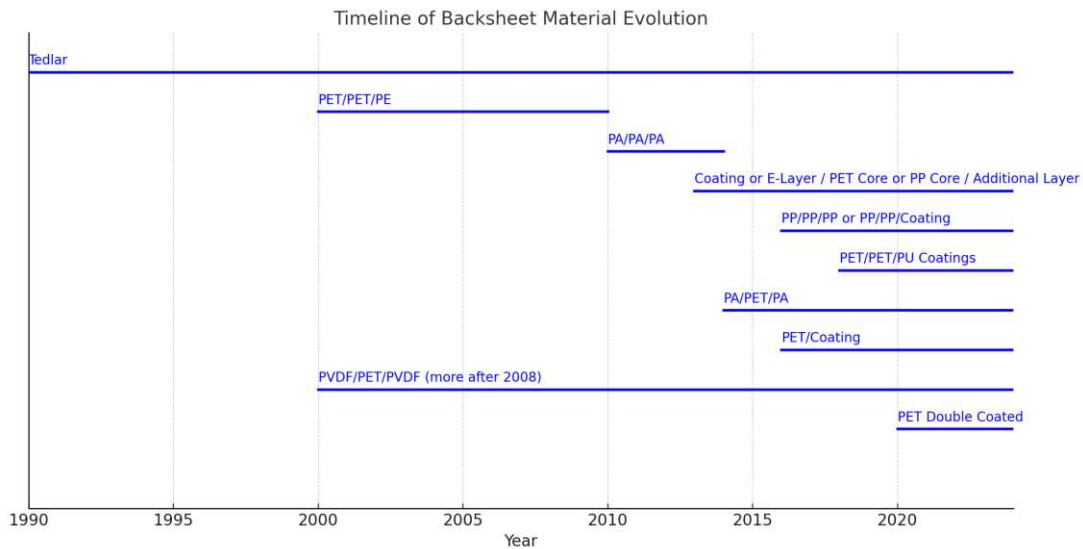


Figure 1.2: Timeline of backsheet material evolution in photovoltaic modules according to Markus Feichtner, Dr. Gabriele Eder and Dr. Gernot Oreski (personal communication at the PVSEC (European Photovoltaic Solar Energy Conference and Exhibition), September 2024). The nomenclature (e.g., PA/PA/PA) represents multilayer structures, where each material separated by a slash (/) corresponds to a distinct layer in the backsheet composition.

There is a wide variety of materials that manufacturers use for multilayered polymer backsheets. Figure 1.2 illustrates the timeline of backsheet material evolution in PV modules. Initially, so-called "Tedlar" backsheets, composed of polyvinyl fluoride (PVF) / PET / PVF, dominated the market. However, starting from the early 2000s, other multilayer and coated backsheets became more prevalent, integrating different polymers and combinations to optimize performance and cost.

Polyethylene terephthalate (PET) has been widely used as a core material in backsheets due to its mechanical strength and relatively low cost. To enhance its weather resistance, PET is often combined with coatings or additional polymer layers. For example, polyethylene (PE) layers are added to improve flexibility and act as perfect tie layer to the encapsulant. Polyamide (PA), known for its strong mechanical properties and resistance to abrasion, is used in multilayer configurations, such as PA/PA/PA, where all layers are polyamide, or in combinations like PA/PET/PA, where PET serves as the core. Polypropylene (PP) is often used

in configurations like PP/PP/PP or as a coated layer, such as PP/PP/Coating. Meanwhile, polyvinylidene fluoride (PVDF), a fluorinated polymer, has been incorporated in some designs (e.g., PVDF/PET/PVDF) due to its exceptional UV stability and resistance to chemical degradation [18].

A key distinction exists between coextruded backsheets and laminated backsheets. Coextruded backsheets, such as PA/PA/PA and PP/PP/PP, consist of polymer layers that are directly fused together during production, creating a seamless structure. In contrast, laminated backsheets feature a core layer – typically PET in the case of Tedlar backsheets – that is bonded using an adhesive to outer protective layers. While coextruded backsheets eliminate potential failure points associated with adhesives, laminated designs allow for greater flexibility in material combinations to optimize performance characteristics [43].

Coatings play a crucial role in modern backsheet designs, providing additional layers of protection against UV radiation, moisture ingress, and mechanical wear. Initially, these coatings contained fluorine for their excellent inertness and thus weathering stability characteristics. However, environmental concerns about fluorine-based polymers especially during the recycling process have led to a gradual reduction in fluorine content over the years [3, 9].

1.3 Typical Failure Modes in PV Modules

Common failure modes in PV modules have been extensively documented, with material degradation playing a significant role. Studies identified backsheet cracking, discoloration of encapsulants, and cell-level defects as the most prevalent issues in globally fielded PV modules [53, 42, 22]. Figure 1.1b shows that backsheet-related defects account for 15 % of total analyzed PV modules, the same percentage as cell/interconnect defects, highlighting the significance of backsheet degradation in module reliability. Environmental stressors such as UV radiation, temperature fluctuations, and mechanical loads are primary contributors to these failures. For instance, backsheet cracking is often linked to prolonged exposure to thermal cycling and UV degradation, particularly in polyamide materials [12]. These failures not only impact module efficiency but also pose safety risks, such as electrical leakage or potential fires [35, 53].

1.4 Polyamide Backsheet Failures

PV-modules with coextruded PA-based 3-layer backsheets were found to develop very distinct failure modes after several years of operation in the field [24, 23, 35]. Cracks in the backsheet, shown later in Figures 4.1 and 4.2, often form above the bus bars due to localized mechanical stress in these areas. The PA backsheet itself successfully passed all aging tests, indicating that the primary issue lies within the multi-material composite structure of the PV module. Due to the varying coefficients of thermal expansion among the different materials, mechanical stresses develop within the module. Since the PA backsheet is fixed within the module structure, it cannot expand freely in the x- and y-directions in response to temperature fluctuations, ultimately leading to crack formation [12].

More generally, cracks in polyamide backsheets result from anisotropic thermal expansion. The coefficients of thermal expansion varies significantly in different directions of the backsheet, causing uneven mechanical stress during daily and seasonal temperature changes. This thermal-mechanical stress accelerates physical aging, reducing the material's plastic deformation capability. Furthermore, internal stresses introduced during the lamination process and structural mismatches in the composite layers of the backsheet contribute to the degradation [12].

In general, three distinct crack types are known [11]:

1. local backsheet cracking caused by individual hot cells or hot spots
2. tile-shaped, square cracks (along the intercellular spacings)
3. longitudinal cracks (beneath the busbars of the cells) – see Figure 4.1

In this study, only the 3rd crack type from this list has been analyzed.

In addition to cracking, two prominent forms of deterioration have been identified in PA-based backsheets: photo-oxidative degradation and surface chalking. Photo-oxidation occurs when the backsheet is exposed to UV light in the presence of oxygen, breaking down the polyamide chains. This degradation leads to the formation of a carbonyl band (C=O) at 1710 cm^{-1} , detectable through infrared spectroscopy [12]. Surface chalking, on the other hand, is linked to the titanium dioxide (TiO_2) particles used for UV protection. While these particles offer initial protection, they can form radicals under prolonged UV exposure, contributing to the breakdown of the polyamide material. Chalking is often observed as an early indicator of more severe damage, such as cracking [17].

1.5 ReNew PV research project

The ReNew PV project addresses an important challenge in the photovoltaic (PV) industry: extending the lifetime of PV modules to ensure their long-term reliability and consequently sustainability. PV modules are designed to operate for over 20 years, which is achieved by 93 % after 15 years of the installed PV modules [28]. However, field studies have shown that from the failed modules a significant 40 % portion of failures are caused by backsheet degradation, particularly cracking, delamination, and loss of electrical insulation resistance [12]. Such failures are critical, as they can lead to system downtime, reduced energy yield and safety risks, especially in humid environments. Dismantling and recycling has been the conventional strategy for these early degraded/failed modules, but repair and reuse offer a more sustainable and economically viable alternative. Notably, between 2010 and 2015 alone, approximately 11–12 GW of PV modules with polyamide (PA) backsheets were installed globally [55], emphasizing the scale of this issue. This thesis focuses on developing repair solutions for damaged backsheets, addressing real-world issues of material degradation while minimizing environmental impact. By restoring the insulation resistance and mechanical integrity of the backsheets, repair solutions extend module lifetimes, reduce waste, and promote circular economy principles in the PV industry. This research thus contributes to a more sustainable energy transition, providing practical solutions for PV operators and stakeholders.

1.6 Research Questions

The objective of this thesis is to compare different backsheet repair solutions in their effectiveness of prolonging the lifetime of a PV module with backsheet cracks and to identify the best repair solution for cracked polyamide backsheets. In pursuit of this objective, this thesis investigates the following research questions:

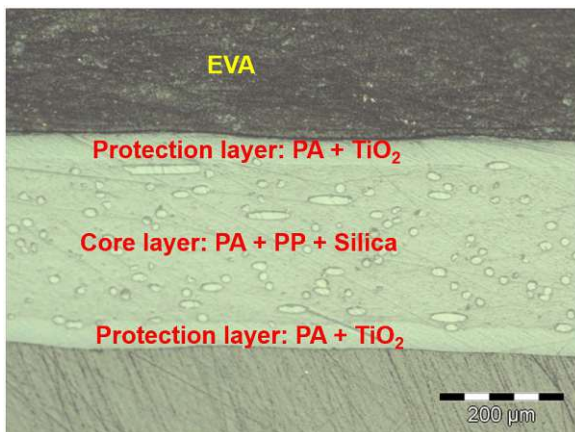
1. **What is the most reliable method for examining the crack-filling effectiveness of repair coatings?**
2. **How do the applied coatings perform under accelerated aging test conditions?**
3. **Which repair approach is most suitable for different types of cracks in PV backsheets?**

Chapter 2

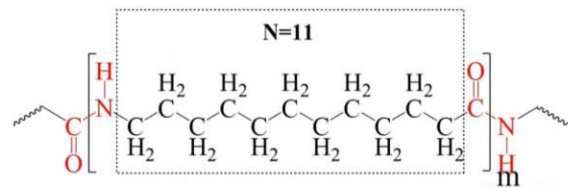
Sample description

2.1 PV Modules with Polyamide Backsheets

The focus of this project is centered around the polymer backsheet of the PV modules, due to the observed failure (cracking) and the potential repair techniques developed to address it. The backsheet in question is a polyamide-based material produced by the former Austrian Backsheet producer Isovoltaic that is known as AAA-backsheet. This backsheet has a co-extruded design, consisting of three layers, all made from polyamide-12 (PA12, see 2.1b), as depicted in Figure 3.1b, which shows the chemical structure of PA12. The central layer of the AAA-backsheet is modified with polypropylene (PP) and reinforced with a silica filler (glass fibers) to improve mechanical strength. Additionally, the inner and outer layers are filled with titanium dioxide (TiO₂), which acts as a UV-protection agent [17]. Figure 2.1a provides a microscopic view of the backsheet cross-section (integrated into a PV module, with the encapsulating ethylene-vinyl acetate (EVA) layer visible on the upper side).



(a) Light microscopy image of the Cross-section of a co-extruded polyamid-backsheet [12]



(b) Chemical structure of polyamide 12 [57]

Figure 2.1: Polyamide backsheet information

2.2 PV Module Specifications and Origin

The PV modules used in this study, Modules 1-5, originate from an open rack rooftop system in Koper, Slovenia. They have been selected due to the presence of cracked backsheets. Modules

6 and 7 are sourced from Greece and show the same cracks in the backsheet.

The front side of the modules is constructed with 3.2 mm tempered solar glass (ESG), and the backsheet is made by Isovoltaic. The modules use Etimex encapsulation materials to protect the cells from environmental exposure. The efficiency of the modules ranges from 14.05% for the 210 Wp model, 14.22% for the 235 Wp model to 14.52% for the 240 Wp model, optimizing the energy output relative to the module size. The area required for each kilowatt of power installed ranges from 7.09 m² for the 210 Wp model to 7.03 m² for the 235 Wp model and 6.89 m² for the 240 Wp model, reflecting their compact and efficient design.

Parameter	Module 1-5	Module 6	Module 7
P _{MPP} (W)	240.00	210.00	235.00
Tolerance	-0% / +3%	-0% / +3%	-0% / +3%
U _{MPP} (V)	29.56	26.47	29.70
U _{OC} (V)	37.33	33.26	37.08
I _{MPP} (A)	8.13	7.96	7.94
I _{SC} (A)	8.80	8.59	8.58
Serial Number (S/N)	60166974	60092641	60089578
Item Number	15755	15264	15700
Max. System Voltage (V)	1000	1000	1000
BS-Type	AAA	AAA	AAA

Table 2.1: Comparison of the electrical characteristics (power P_{MPP}, voltage U_{MPP} and current I_{MPP} at the maximum power point; open-circuit voltage U_{OC} and short-circuit current I_{SC}) of the modules according to the type label of Module 1-5 (240Wp), Module 6 (210Wp) and Module 7 (235Wp) specifications.

Chapter 3

Characterization Methods

This chapter presents the methods used for the electrical and material characterization and evaluation of PV modules in three different states:

- **Defective:** Modules before repair
- **Repaired:** Modules after the repair process
- **Repaired and aged:** Modules that have undergone repair and the subsequent accelerated aging test

By analyzing changes in the characterization parameters due to repair and accelerated aging, conclusions can be drawn regarding their impact on electrical performance and material stability. Each method is described in detail, including its principles, relevance, and applicability to the analysis of backsheet degradation and repair effectiveness.

3.1 Visual Inspection and Microscopy

3.1.1 Visual Inspection

Visual inspection is one of the most simple but most important characterization methods, as it provides a quick and efficient assessment of the module's condition, serving as a solid basis for further analysis. Most defects in both, repaired and unrepaired backsheets (BS) can be identified visually, particularly when the inspection is performed by an experienced individual with knowledge of common failure patterns. Visual inspection allows for the identification of cracks, delamination, discoloration, chalking and other surface irregularities, which are critical indicators of backsheet degradation or repair quality. Its simplicity and effectiveness make it an essential first step in the characterization process.

3.1.2 Light Microscopy

A small handheld light microscope (PCE-MM 800 digital microscope), which can be connected to a laptop via USB for live video streaming, has proven to be a convenient and effective tool for gaining insights into the surface phenomena on a microscopic scale (magnification of x20 and x200) [44]. Its ease of use and its portability make it particularly suitable for quickly identifying finer details like microcracks on the backsheet surface that may not be visible during standard visual inspection by the naked eye.

For larger image sections and improved image quality (up to 128x optical magnification [41]), a stationary light microscope (olympus SZH) was used. In this project, it was primarily employed to analyze cross-sections of the defect or repaired BSs. This allows for an effective visualization of crack type and crack filling. To prepare the samples, the module piece was embedded in epoxy resin, ground, and polished until it was level with the resin surface. This preparation method not only facilitates cross-sectional analysis under the light microscope but also enables Attenuated Total Reflection Infra Red (ATR-IR) imaging, which will be described in Section 3.2.

3.1.3 Ultrasonic Microscopy

Ultrasonic microscopy covers a wide range of techniques that use high frequency sound waves to probe and image the internal structure of materials. The field encompasses a variety of methods operating at different frequency ranges, allowing both surface and subsurface imaging with resolutions down to the microscopic scale. One of the most widely used forms of ultrasonic microscopy is Scanning Acoustic Microscopy (SAM), which uses focused ultrasonic waves to scan a sample in a raster pattern. While ultrasonic microscopy refers to any method that uses ultrasound-based imaging, SAM is unique in its ability to produce high-resolution, non-destructive images by scanning the surface and internal features of a material. Through the interaction of sound waves with different material interfaces, SAM can detect variations in properties such as acoustic impedance, making it a powerful tool for materials analysis [34]. For this study a PVA TePla SAM 400 was used. It operates at frequencies ranging from 10 MHz to 400 MHz [36].

Acoustic Impedance and Reflection at Interfaces

The primary physical principle underlying SAM is the interaction of *ultrasonic waves* with the material interfaces. When an ultrasonic wave encounters an interface between two materials with different *acoustic impedance*, part of the wave is reflected, and part is transmitted.

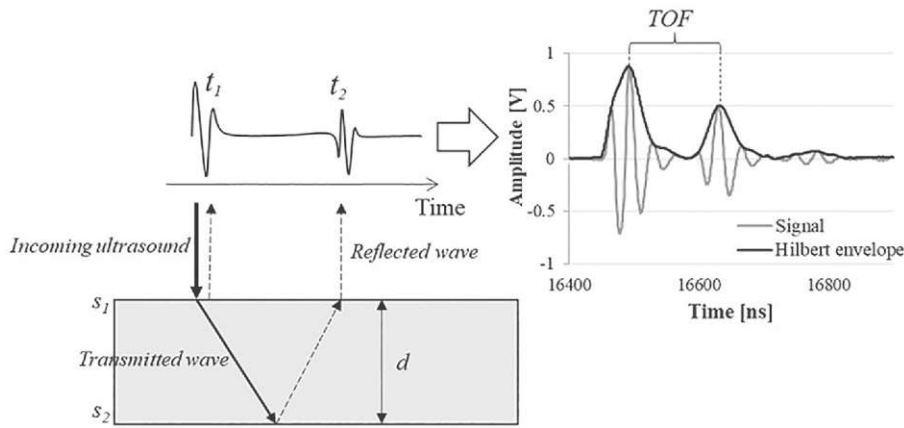


Figure 3.1: Measurement principle of the scanning acoustic microscopy in reflection mode [37]

The *acoustic impedance* Z of a material is defined as:

$$Z = \rho v \quad (3.1)$$

where:

- ρ is the material's *density*,

- v is the *speed of sound* in the material.

The reflection coefficient R , which quantifies the fraction of the wave that is reflected at the interface between two materials with impedances Z_1 and Z_2 , is given by:

$$R = \frac{Z_2 - Z_1}{Z_2 + Z_1} \quad (3.2)$$

In the case of PV backsheets, the polymer layers and busbars have distinct acoustic impedance, resulting in measurable reflections. By analyzing the reflected wave signals, it is possible to localize and quantify subsurface defects such as *cracks*, *voids*, or *delamination*.

Ultrasonic Wave Propagation and Resolution

The *resolution* of SAM is determined by the wavelength λ of the ultrasonic waves, which is related to the frequency f and the speed of sound v by:

$$\lambda = \frac{v}{f} \quad (3.3)$$

Higher frequencies provide better lateral and axial resolution, allowing for more precise imaging of fine cracks within the backsheet. However, as frequency increases, the *attenuation* of the ultrasonic waves also increases, limiting the depth of penetration [46]. In typical polymer applications, *frequencies in the range of 50-200 MHz* are used to balance resolution and penetration depth, which is suitable for probing thin polymer layers and detecting cracks at the busbar-cell interface.

Attenuation and Wave Scattering

As ultrasonic waves travel through a medium, they experience *attenuation* due to absorption and scattering. The attenuation coefficient α , which describes the exponential decay of wave amplitude as a function of distance x , is given by:

$$A(x) = A_0 e^{-\alpha x} \quad (3.4)$$

where $A(x)$ is the wave amplitude at distance x , and A_0 is the initial amplitude. Materials with inhomogeneous structures, such as the multi-layered PV backsheets, may cause significant *scattering* of the ultrasound waves, which complicates the interpretation of the reflected signals.

The attenuation coefficient α can also be expressed as a function of angular frequency ω following a power-law relationship observed in many viscoelastic materials, including polymers:

$$\alpha(\omega) = \alpha_0 \omega^\eta \quad (3.5)$$

where α_0 is a material-specific constant, and η is a non-negative frequency-dependent exponent obtained from experimental data. This relationship highlights how higher frequencies lead to greater attenuation, as observed in ultrasonic applications. For a given wave propagation distance Δx , the pressure $P(x)$ of the wave decreases exponentially, as described by:

$$P(x + \Delta x) = P(x) e^{-\alpha(\omega)\Delta x} \quad (3.6)$$

In the case of multi-layered PV backsheets, the attenuation is further influenced by internal interfaces and material discontinuities, which amplify scattering effects. These complexities underscore the need for precise modeling and frequency selection in ultrasonic characterization to minimize signal loss and improve the accuracy of defect detection.[50].

Time-of-Flight and Crack Depth Measurement

The *time-of-flight* (*ToF*) technique is a critical aspect of SAM used to determine the depth of subsurface features. The time taken for the ultrasonic wave to travel from the transducer, reflect off an interface, and return to the detector is related to the distance d from the surface to the defect by:

$$d = \frac{v \cdot t}{2} \quad (3.7)$$

where t is the measured ToF, and v is the speed of sound in the material. By applying this technique, we can precisely determine the depth of cracks within the backsheets. The accuracy of this measurement depends on the precise knowledge of the sound velocity in each material layer, which can vary between different polymers and metal components.

Limitations of Scanning Acoustic Microscopy

While SAM provides valuable insights into subsurface defects, several limitations exist for its application in analyzing PV backsheets. First, in the setup used for this study, SAM is unable to resolve *microcracks* due to either its resolution limit or insufficient contrast. The resolution limit ranges from 50 μm to 5 μm at frequencies of 40 MHz to 400 MHz [34]. Additionally, due to the unknown phase velocity of sound in some of the backsheet materials, and the difficulty in determining the exact distance from the transducer to the sample surface - especially in the presence of uneven surfaces - quantitative analysis is not feasible for this specific application. Nevertheless, *qualitative analysis* is still possible, allowing for general characterization of the crack depth and distribution. In order to transmit the sound signal into the backsheet, a coupling medium is required to facilitate the transfer of ultrasonic waves from the transducer to the surface. Without a coupling medium, the signal would need to cross an air gap, which would result in strong reflection and signal loss due to the large acoustic impedance mismatch between air and solid materials [34]. To ensure efficient signal transmission, deionized water is used as the coupling medium in this study, providing a consistent interface between the transducer and the backsheet.

Moreover, assessing the quality of crack filling in coated backsheets did not yield sufficient accuracy in the setup used for this study, limiting the method's effectiveness for this particular measurement.

3.2 Infrared Spectroscopy (IR)

The basic principle of spectroscopy relies on the interaction between electromagnetic waves and matter. Infrared (IR) spectroscopy, in particular, examines how IR radiation interacts with molecular structures, exciting their vibrational modes. These vibrational modes, which are unique to molecular bonds and structures, allow for the identification of organic and polymer molecules [20, 7].

When a molecule absorbs a photon with a specific frequency (ν), it transitions to a higher vibrational state, provided the energy conservation law is satisfied:

$$E_i - E_k = h \cdot \nu_{ik}$$

where h is Planck's constant. Only specific frequencies that match the molecule's vibrational energy levels are absorbed, producing characteristic absorption peaks in the IR spectrum [10].

These peaks help identify functional groups such as C=O, O-H, and N-H, as well as entire molecular structures.

Not all vibrational transitions are detectable. Selection rules derived from quantum mechanics dictate that only vibrations inducing a dipole moment change are IR-active. This makes polar bonds such as C=O and O-H particularly significant in IR spectroscopy [48, 10].

Traditional IR spectroscopy in transmission mode requires extensive sample preparation, often necessitating thin films of 20 μm to 50 μm . This mode operates in the mid-infrared (MIR) range, spanning wavelengths from 2.5 μm to 25 μm (4000 cm^{-1} to 400 cm^{-1}).

FTIR spectroscopy builds on these techniques by employing an interferometer to collect data across a wide range of IR wavelengths simultaneously. This approach enhances speed, sensitivity, and resolution, making it a versatile tool for analyzing various materials.

In transmission mode, where IR light passes through the sample, the absorption and transmission relationship is governed by Lambert-Beer's law:

$$I = I_0 e^{-\alpha d}$$

where I is the transmitted light intensity, I_0 is the incident light intensity, α is the absorption coefficient, and d is the sample thickness. The absorption coefficient reflects the characteristics of specific molecular vibrations, making this mode ideal for simple and homogeneous samples, albeit limited by sample thickness and absorption characteristics [21].

In this project, only the Attenuated Total Reflection (ATR) method was used, as it offers significant advantages for analyzing backsheet materials and repaired sections with minimal sample preparation.

ATR-IR is a sampling technique within Fourier-transform infrared (FTIR) spectroscopy that utilizes an ATR crystal with a high refractive index (e.g., diamond or germanium). Infrared light is directed into the crystal, where it undergoes total internal reflection at the crystal-sample interface. At each reflection, an evanescent wave penetrates a shallow depth into the sample surface, typically between 0.5 μm to 3 μm . The absorbed portion of this wave provides spectral data specific to the sample's molecular vibrations [21].

Compared to traditional transmission IR spectroscopy, ATR-IR offers:

- Minimal or no sample preparation, as solids, liquids, or powders can be analyzed directly.
- Surface-sensitive analysis, particularly useful for coated backsheets or fine crack regions.
- The ability to handle hard, rough, or thick samples that cannot be prepared as thin films.
- Mobile ATR-IR Device: Portable, handheld IR spectrometer equipped with ATR sampling head allowed for on-site measurements and quick assessments of the backsheet surfaces. This device is especially useful for identifying (i) the backsheet material on different location of the module, e.g. close to cracks or defects, and (i) of the coating material directly on the PV module.
- ATR-IR Imaging Systems: Stationary IR spectrometers with ATR-IR imaging capabilities were used for more detailed, high-resolution analysis of cross-sectional samples. This technique enables spatially resolved chemical imaging, allowing the observation of variations in material composition across the crack regions or repair layers.

3.2.1 IR Spectrometer

An infrared (IR) spectrometer is a device used to measure the absorption of infrared light by a material, revealing detailed information about its molecular composition. The basic com-

ponents of an IR spectrometer include a light source, an interferometer (in the case of FTIR spectrometers), a sample holder, and a detector [21].

The light source typically emits broad-spectrum infrared radiation, which is directed through the interferometer. In FTIR spectrometers, the interferometer modulates the infrared light by splitting it into two beams: one passing through a fixed mirror and the other through a moving mirror. The beams are then recombined, creating an interference pattern that varies with the position of the moving mirror. This interference pattern contains all the information of the sample's absorption over a wide range of wavelengths [21].

The modulated infrared light is then directed toward the sample, where specific wavelengths are absorbed depending on the molecular vibrations of the sample. The transmitted light is detected by a sensitive detector, usually a mercury cadmium telluride (MCT) or deuterated triglycine sulfate (DTGS) detector, depending on the wavelength range and required sensitivity. The detector measures the intensity of light at each wavelength, creating an interferogram [21]. The interferogram is subsequently processed using a Fourier transformation, converting the raw data into a spectrum. The resulting spectrum shows the intensity of absorption at various frequencies, corresponding to different molecular vibrations within the sample.

For this project, two types of devices were employed to analyze the backsheet materials: (i) a portable spectrometer in ATR-IR-mode (A2 technologies, Exoscan) was in use for the surface sensitive measurements on the backsheet surface and (ii) a desktop system IR-Microscope-spectrometer of Perkin Elmer (Spotlight 3) for the ATR-IR-imaging measurements were used.

The IR measurements conducted with the Exoscan device employed a diamond ATR crystal brought into direct contact with the sample surface (either the backsheet or the coating). The ATR (attenuated total reflection) technique is a surface-sensitive method that investigates only the top 1.5 μm to 2.5 μm of the sample, providing detailed insights into the chemical composition of the outermost layers [1].

3.3 Electrical Characterization

In order to evaluate the effectiveness of backsheet repair, it is crucial to assess the electrical performance and condition of the PV modules. Accurate measurement of electrical parameters is essential to determine the degree of degradation and ensure that the repair process has not caused any damage to the electrical current carrying components. In this section, we focus on three key electrical measurements that provide a comprehensive understanding of the module's state:

3.3.1 Power Measurement

In PV modules, the *current-voltage (I-V) measurement* is one of the most fundamental method to assess the electrical performance of a module. The I-V curve represents the relationship between the current (I) generated by the module and the applied voltage (V), providing a comprehensive view of the module's electrical behavior under specific conditions [19].

An I-V curve is obtained by sweeping the voltage across the module terminals and simultaneously measuring the resulting current. This curve allows for the extraction of critical parameters such as:

- *Short-circuit current* (I_{SC}) – The maximum current when the voltage is zero.
- *Open-circuit voltage* (V_{OC}) – The maximum voltage when the current is zero.
- *Maximum power point* (P_{max}) – The point where the product of voltage and current is at its maximum.

- *Voltage at maximum power point (U_{MPP})* – The voltage at which the module produces its maximum power.
- *Current at maximum power point (I_{MPP})* – The current at which the module produces its maximum power.
- *Fill factor (FF)* – A measure of the 'squareness' of the I-V curve, which indicates the quality of the module.
- *Efficiency* – the portion of energy in the form of sunlight that can be converted via electricity by the solar cell.

These parameters describe the electrical performance of the PV-module and their changes offer insights into the degree of degradation or damage within the electrical circuit in the module. Any significant deviation from the expected values may indicate issues such as *cell cracks* or *interconnection faults*. Regular I-V measurements play a crucial role in monitoring the health of PV modules over time, allowing early detection of performance losses. By performing measurements before and after the accelerated aging test, the effectiveness of the repair solutions can be evaluated. A lower degradation rate in repaired modules compared to untreated ones would indicate a beneficial impact of the repair strategy on the longevity of the module.

In this work, an I-V-400w from HT Instruments was used for the I-V measurements. It is a versatile device that allows for a rapid and precise evaluation of the electrical performance of PV modules and strings, making it ideal for field applications. The device features automatic testing modes and compatibility with various environmental sensors to account for irradiance and temperature, ensuring accurate I-V curve tracing under real conditions [26].

Table 3.1: Key Parameters of the I-V-400w from HT Instruments

Parameter	Specification
Maximum Voltage (V_{max})	1000 V DC
Maximum Current (I_{max})	15 A
Power Measurement Range	0.1 kW to 10 kW
Measurement Accuracy	$\pm 1\%$
Irradiance Measurement Range	100 W/m ² to 1200 W/m ²
Temperature Measurement Range	-10°C to 85°C
Data Storage	300 I-V curves
Communication Interface	USB / Bluetooth

The I-V-400w includes several features that enhance its functionality for field testing:

- **Real-time irradiance and temperature compensation** – This feature converts I-V curve measurements taken under current environmental conditions to standard test conditions (25 °C cell temperature and 1000 W m⁻², as per IEC 60891), improving the accuracy of the results.
- **Auto-recognition of PV modules** – The device can identify the connected PV module type and adjust its measurement parameters accordingly, simplifying the setup process and ensuring appropriate test settings.

These functionalities enable efficient testing of PV modules in the field, providing valuable insights into electrical performance and potential degradation or cell damage, particularly after backsheet repair.

3.3.2 Electroluminescence Measurement

Electroluminescence (EL) measurements are a critical technique for studying the electronic properties and defect states in semiconductors and optoelectronic devices. The process of EL occurs when an electric field applied to a material leads to the recombination of electrons and holes, resulting in the emission of photons. Semiconductors are materials whose electrical conductivity lies between that of conductors and insulators. Their conductivity is primarily determined by the presence of a bandgap, an energy range within which no electronic states exist. At absolute zero temperature, electrons occupy the lower-energy valence band, while the higher-energy conduction band remains empty. When energy is supplied (e.g., through an applied voltage or light absorption), electrons can be excited from the valence band to the conduction band, leaving behind positively charged vacancies known as holes. These electron-hole pairs play a crucial role in semiconductor operation. This phenomenon is governed by the principles of band theory, where the energy difference between the conduction and valence bands determines the wavelength of the emitted light, following Planck's relation $E = h\nu$ (where E is the photon energy, h is Planck's constant, and ν is the frequency of the emitted light) [31].

The efficiency of EL is also highly dependent on the material properties of the semiconductor, such as the presence of impurities or defects, which can act as non-radiative recombination centers, reducing the quantum efficiency of photon emission [51]. In addition, the EL spectrum and intensity can provide insights into the band structure, defect levels, and internal electric fields within the device, making it a valuable tool for characterizing LEDs, laser diodes, and solar cells [38]. By analyzing the EL images (spectra mapped spatially across a device), researchers can diagnose spatial non-uniformities and assess material quality, which is essential for improving device performance and longevity.

EL imaging is a rapid, non-destructive technique for detecting cell cracks, inactive regions, and other defects that impair the performance of PV modules. By applying a forward bias to the module, the p-n junction of the solar cells becomes conductive, allowing current to flow through the device and generating electroluminescence (EL) as electrons and holes recombine, releasing energy in the form of photons [45]. Healthy areas of the PV cell emit light uniformly due to consistent electron-hole recombination, while defective regions, such as cracks, broken interconnections, or areas with elevated resistive losses, appear darker or exhibit irregular patterns. These disruptions reduce local light emission by hindering current flow and recombination. EL measurements are widely used to evaluate the effects of environmental stressors on cell performance, providing valuable insights in both laboratory and field testing [15, 2].

3.3.3 Insulation Resistance Measurements

Insulation resistance (R_{iso}) measurements are essential for assessing the electrical safety and durability of PV modules, particularly in humid field environments where leakage currents are prone to increase. In PV modules, electrical insulation is primarily provided by the front and backsheets, which separate the current-carrying interconnections from the external environment. Leakage currents in PV modules result from compromised insulation, which can lead to efficiency losses and safety hazards and electric shock risks [52, 30]. A cracked backsheet (BS) can result in current leakage, posing a significant safety risk under certain conditions. For example, modules with cracked and wet or moist backsheets exposed to morning sunlight may experience such leakage. The moisture could originate from rain or dew. This behavior was reported by the project partner ENcome, a company specializing in Operations and Maintenance (O&M) of PV systems. This can be observed because modern inverters measure the insulation resistance of PV modules and shut down if the resistance falls below a critical value therefore resulting in reduced energy output of the PV module [6].

The wet leakage test was performed on the basis of the guidelines outlined in IEC 61215-2:2021 (MQT 3) [27]. According to this standard, a minimum insulation resistance of 24 M Ω

is required to pass the test. For the experiment, several liters of water were poured over the BS, and the setup was left for two minutes. A voltage of 1000 V was then applied, and the resistance between all the current-carrying elements (e.g. cells and bus bars), and the water was measured.

Chapter 4

Backsheet Repair: Methodology and long-term Stability

This chapter focuses on the investigation and evaluation of repair methods for PV modules with cracked BS, aiming to restore insulation integrity and improve module durability.

The development of a repair methodology was conducted in two phases. In the initial phase, potential repair materials - coatings and tapes - were tested in small sample sections of BS on a single module. This approach allowed for a detailed analysis of BS crack filling including the use of destructive methods such as cutting sample parts and preparing cross sections. By assessing the filling effectiveness on smaller samples, we were able to refine the repair method before applying it to intact, full-sized modules in the next phase.

In the second phase, each repair method was applied to one of seven full-sized PV modules with cracked BS. These modules were then subjected to temperature cycles within a climate chamber to simulate accelerated aging. This testing approach was designed to evaluate the reliability of the repaired backsheets under controlled environmental conditions, effectively mimicking the thermal stresses that PV modules encounter over years of field exposure. The findings from these experiments contribute valuable insights into the viability of BS repair strategies for extending module service life, offering practical implications for maintaining PV system reliability.

Another crucial preparatory step before applying any coating or tape is the thorough cleaning of the backsheet. Over years of field exposure, the backsheet accumulates dust, dirt, and other contaminants that interfere with adhesion. Additionally, chalking, a common degradation phenomenon in aged backsheets, results in a powdery surface layer that further prevents coatings and tapes from adhering properly. Proper surface preparation is essential to ensure strong adhesion and long-term durability of the repair materials. The cleaning process is performed using water and a cleaning cloth and takes approximately three minutes per module. It is essential to allow the backsheet to fully dry before proceeding with any further steps to ensure optimal adhesion of the repair materials.

4.1 Repair Materials and their Application to the Backsheet

Two coating-based materials and one tape-based material were selected as repair solutions. The materials listed in Table 4.1 were selected to test their effectiveness in filling cracks in PV module backsheets, balancing ease of handling and repair quality. The materials used in this study were either provided by project partners (e.g., Remisol) or sourced from commercially available products (e.g., DOWSIL™ PV-9001 and 3M™ Wrap Tapes).

Table 4.1: Overview of repair materials (Abbreviations: RT: Room Temperature; 1-K: 1 component system; 2-K: 2 components system).

Coating	Material Type	Solvent	Curing
DOWSIL™ PV-9001 Backsheet Coating	Silicone	-	1-K, RT
Remisol PV Repair Coating by Kansai-Helios	Cover Coating with Fluorine	Crack Filler: 39.8% (+5%) ¹ ; Cover Coating: 37.8%	2-K, RT
Optimized Remisol PV Repair by Kansai-Helios	Cover Coating without Fluorine	Crack Filler: 39.8% (+5%) ¹ ; Cover Coating: 37.8%	2-K, RT
PVC Foil with Acrylic Adhesive	PVC	-	-

¹ An additional 5% solvent was added to decrease viscosity for easier handling and increased crack filling effectiveness.

- The Remisol PV Repair Coating by Kansai-Helios comprises of two-component systems and is designed to be applied in two steps: (i) crack filling and (ii) a cover (barrier) layer. The crack filler is specifically designed to penetrate and fill cracks effectively, creating a stable foundation for the repair. 0 to 5% of additional diluent can be added to both crack filler and cover coating if the viscosity is too high. After applying the crack filler, sufficient curing time is required to ensure that it hardens enough to resist deformation during the application of the cover coating. This curing time depends on the thickness of the applied layer. A curing time of three hours was chosen to lower the risk of deforming the crack filling layer. Once adequately hardened, the cover coating can then be applied to provide additional protection, completing the repair process.
- The silicone coating is much simpler to apply, as it is a single-component material that requires only one layer. This eliminates the need for multiple applications or curing stages, streamlining the repair process.
- The 3M™ Wrap Foil requires no preparation of the material itself aside from cutting it to the correct dimensions. However, it can be challenging to apply without trapping air bubbles between the foil and the BS. Additionally, precisely cutting around the junction box is not straightforward, and it is difficult to avoid leaving a small gap along the edges of the foil.

4.2 Crack Filling Analysis

In the following section, the effectiveness of repair materials in filling the cracks in the BS is examined. One of the key factors in achieving a successful backsheet repair is ensuring that the cracks are effectively filled. Each cavity represents a potential hazard, as it can trap moisture,

which can, over time, penetrate further into the BS and contribute to its degradation [47, 39]. To investigate the crack filling, both non-destructive and destructive methods are used, with an analysis of the informative value of each approach.

A PV module (see Figures 4.1 and 4.2), featuring an aged polyamide BS in a degraded state was used for the experiment.



Figure 4.1: Overview of the Kioto 235Wp PV module with cracked BS. The numbers refer to the sample areas where the four repair materials were applied

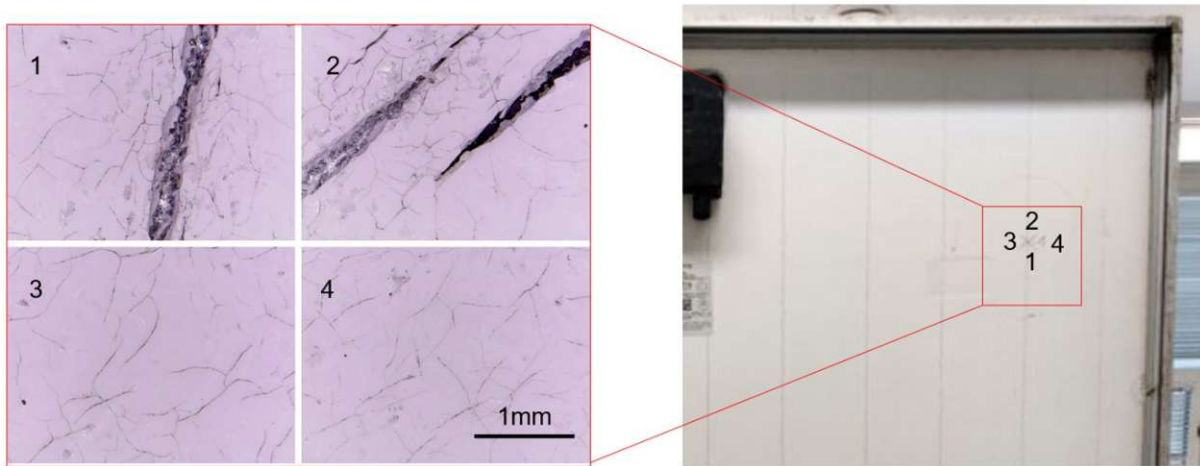


Figure 4.2: LM images taken with the handheld USB microscope (left) of one of the sample areas shown in Figure 4.1.

The experiment involved the application of the repair materials on specific sections of the modules cracked BS (see Figure 4.1):

1. Polyurethane Coating: Remisol PV Repair

- crack filler (applied with a spatula mainly over the cracks) + cover coating (200 μm layer applied with a coating knife)

2. 3M Tape White (Type 1080)

- Application with light pressure
- Application with strong pressure

3. 3M Tape Transparent

- Lightly pressed application
- Strongly pressed application

4. Silicone Coating: DOWSIL™ PV-9001 Backsheet Coating

- 200 μm layer applied with a spatula

The coating areas on the BS were positioned in the corners (see areas 1-4 in Figure 4.1) of the sample module to facilitate Scanning Acoustic Microscopy (SAM), as the device can only accommodate samples with certain dimensions. Each coated section was analyzed using various methods, including SAM as well as LM and ATR-IR imaging in cross section.

4.2.1 Descriptions of the Coating Process

The coating process involved several steps to apply various repair materials on designated areas of the BS of the sample module for testing (example images are shown in Figure 4.3):

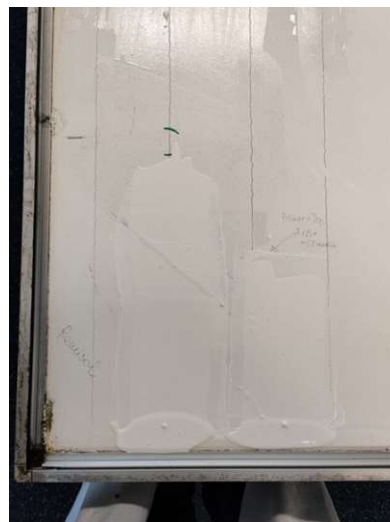
- **Remisol Application:** The crack filler was prepared by mixing 50 g of crack filler prepolymer, 8 g of hardener, and 2 g of solvent. Both, the crack filler prepolymer and the hardener were shaken before opening, leading to unwanted air bubbles. This step was improved in the following coating applications by thoroughly stirring the components with a wooden stick. The mixture was then applied with a plastic spatula to the marked area in

the first corner of the sample module. The crack filler was left to dry for approximately three hours before the next layer was applied. The cover coating was mixed with 50 g of cover coating prepolymer and 3.8 g of hardener, without any solvent. It was applied using a coating knife to achieve a 200 μm layer thickness.

- **Silicone Application:** In the fourth corner of the sample module, on a defined area DOW PV-9001 silicone was also applied with the coating knife to ensure a consistent layer of 200 μm .
- **3M Tape Application:** In the third corner of the sample module, a defined area of the opaque 3M tape was pressed firmly onto the BS, while in the second corner, the same tape was applied with only the protective film lightly pressed down.



(a) Crack filler mixing and application process



(b) Cover coating application with coating knife



(c) Coating knife used for applying coating with specific layer thickness

Figure 4.3: Overview of Coating Processes and Tools

4.2.2 Non-Destructive Measurements: Scanning Acoustic Microscopy (SAM)

In this section, a comparison of the SAM images of the uncoated, but cracked backsheet of an aged PV module and the four coated corners of the sample module will be made. Additionally, the effectiveness of the SAM method for analyzing crack filling will be evaluated.

The SAM scan of the uncoated BS, with the deep crack clearly visible, is shown in Figure 4.4. The three images on the right display cross-sectional scans of the BS along the horizontal lines indicated in the left image that is showing a surface scan. These scans reveal the interfaces within the BS where the acoustic signal is reflected. The first, and thus strongest, reflection occurs at the water - surface interface. Due to noise in the signal in this layer, the deep crack is difficult to see, which suggests degradation of the polyamide layer, as indicated by the presence of numerous microcracks shown in Figure 4.2. The second reflection occurs at the polyamide - encapsulant interface, where the encapsulant surface within the deep crack also appears to be damaged. The following reflection reveals the busbar embedded within the encapsulant in the intercell gap. The final reflection, already significantly weaker, corresponds to the encapsulant - silicon cell interface.

Following the discussion of the SAM results on the uncoated BS, we proceeded to analyze the first coated corner, which uses the PU coating shown in Figure 4.5. The imaging setup

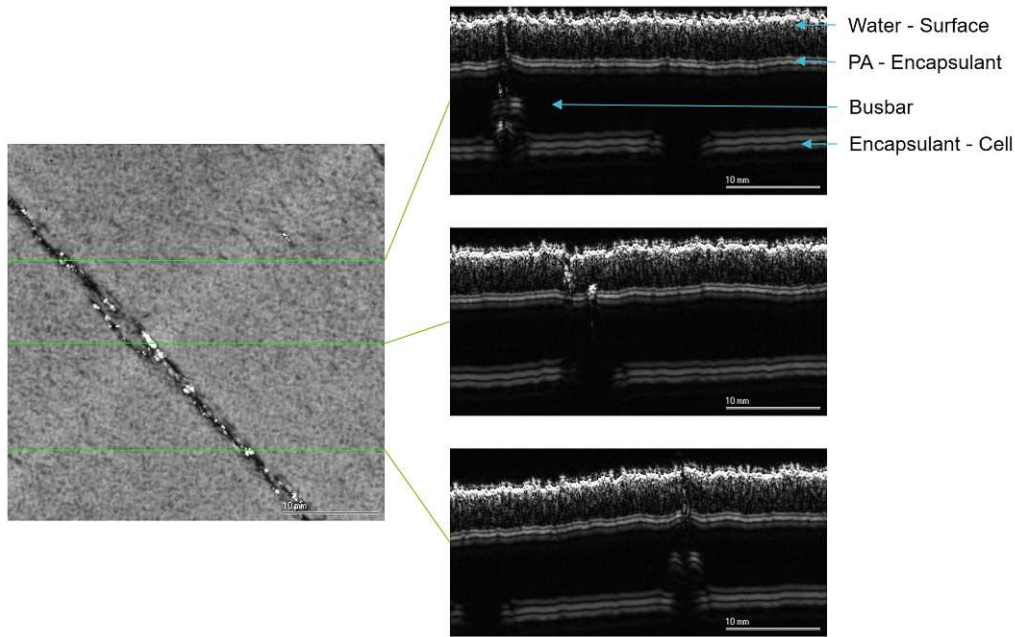


Figure 4.4: SAM images of the uncoated BS: On the left, the image of the area scan of the surface layer; On the right, the cross sectional scans of the BS.

remains the same as in the uncoated BS; however, the surface scan (left image) here captures two distinct areas: one covered by the top coating only (bottom) and another where both, crack filler and top coating are applied (top), allowing for direct comparison. The difference in gray scale levels is attributed to uneven surface heights, as observed in the top interfaces within the cross-sectional scans.

Below the coating's surface, the three interfaces correspond to the same interfaces identified in the uncoated BS: the water-polyamide, polyamide-encapsulant, and encapsulant-silicon cell. A notable feature in this scan is the black dot in the center of the top interface, which indicates the presence of a gas bubble. The cross-section reveals how the bubble prevents the acoustic signal from reaching the underlying material, a result of total internal reflection occurring at the boundary between media with differing propagation velocities.

Despite these observations, it is not possible to determine how effectively the coating has filled the crack. This limitation is partly due to the high refraction angle of the reflected sound waves when they encounter surfaces tilted significantly away from the direction of signal propagation (at angles much lower than 90 degrees). As a result, the reflected signals do not travel back to the sensor, preventing accurate analysis of the crack filling.

Corners 2 and 3 of the sample module were covered with a tape layer. The SAM images are shown in Figure 4.6 with a surface scan on the left and cross-sectional scans on the right. The cross-sectional scans reveal that the signal was unable to reach the BS, which can be explained by the presence of excessive air between the tape layer and the BS. This air layer caused total internal reflection, as discussed in the previous section, preventing the ultrasound signal from passing through to the BS. The dark spots visible in the left image represent areas where the ultrasound signal was able to penetrate into the BS, indicate limited contact between the tape and the BS in these regions.

In Figure 4.7, the SAM images of the cracked backsheet with a silicone layer applied are shown. The results are similar to those observed with the PU coating. The interfaces visible in the cross-sectional scans are, from top to bottom: the silicone surface, the silicone-BS interface, the BS-encapsulant interface, the bus bar embedded in the encapsulant above the intercell gap, and finally the encapsulant-cell interface. The image on the left shows an areal scan of the

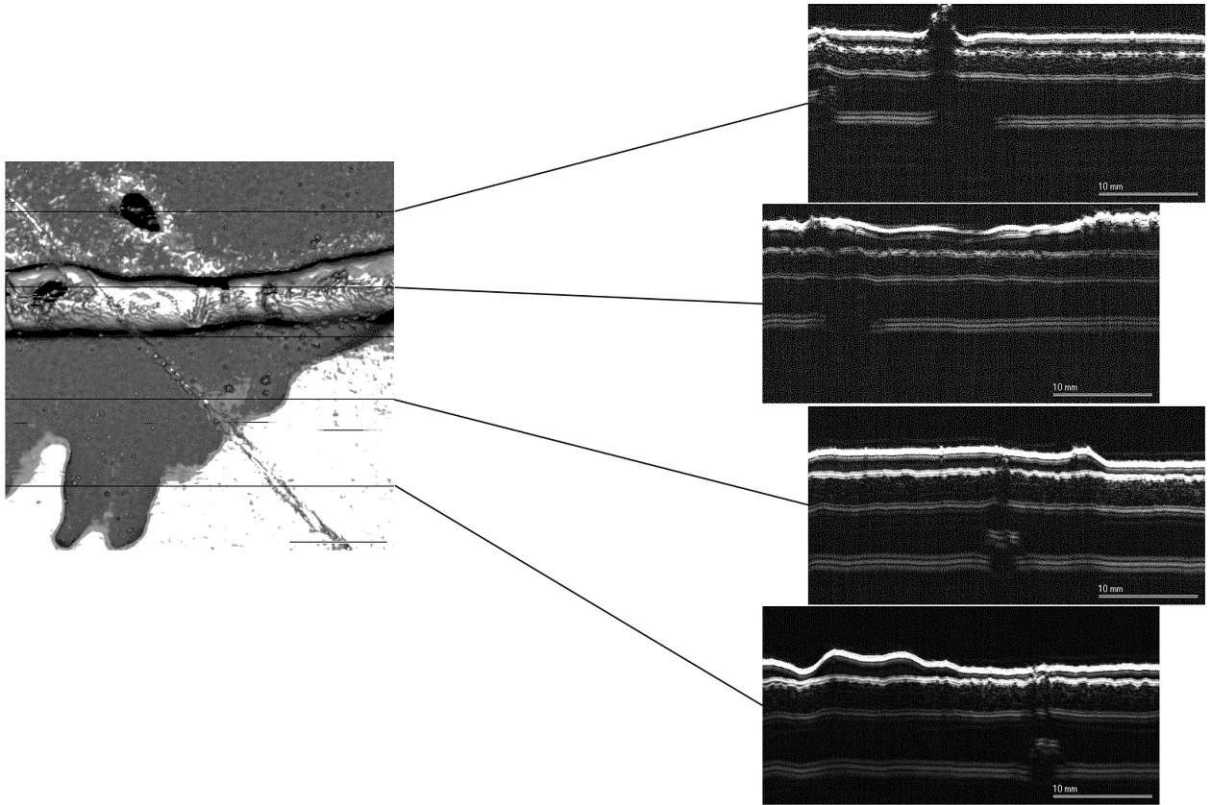


Figure 4.5: SAM image of the BS coated with PU: On the left, the image of the area scan of the surface layer; On the right, the cross sectional scans of the BS.

encapsulant-cell interface, which displays the interface in the plane.

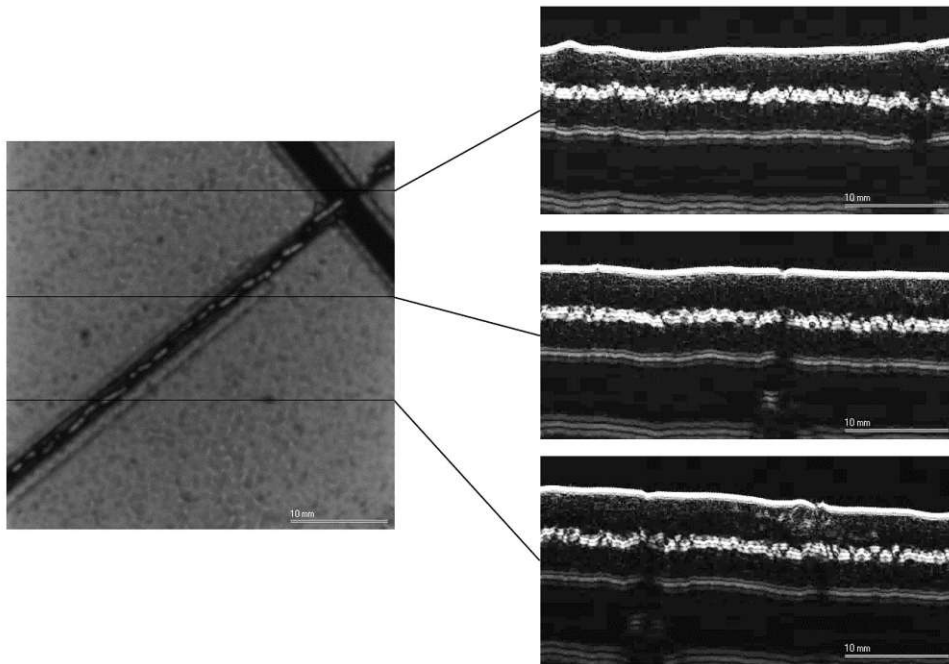


Figure 4.7: SAM images of the BS coated with silicone (DOWSil): On the left, the image of the area scan of the solar cell layer; On the right, the cross sectional scans of the BS.

One significant limitation of the SAM method was its inability to reliably evaluate the

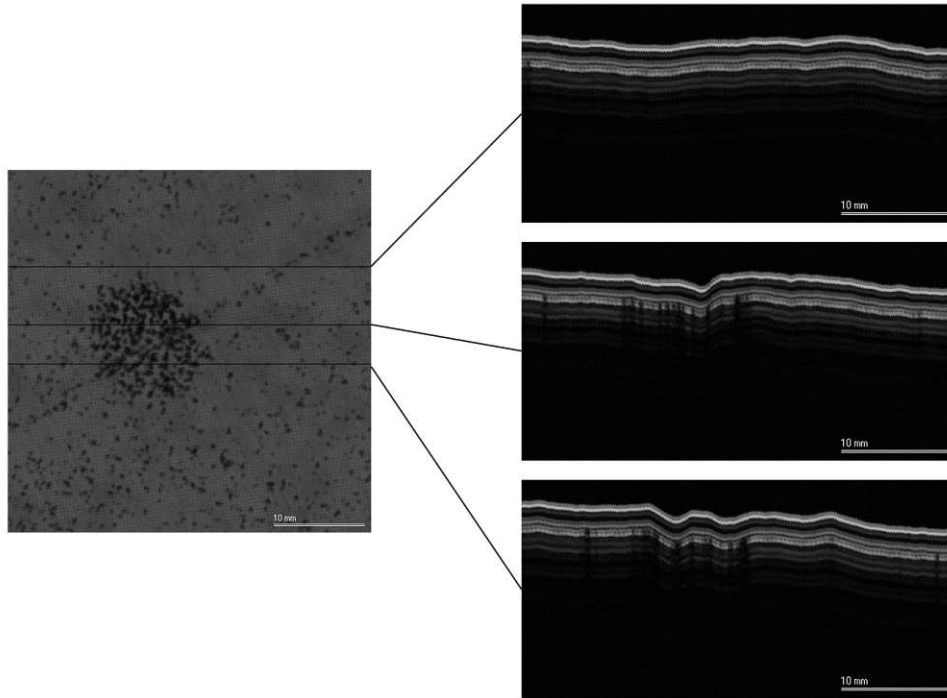


Figure 4.6: SAM image of the BS with tape (3M 1080): On the left, the image of the area scan of the surface layer; On the right, the cross sectional scans of the BS.

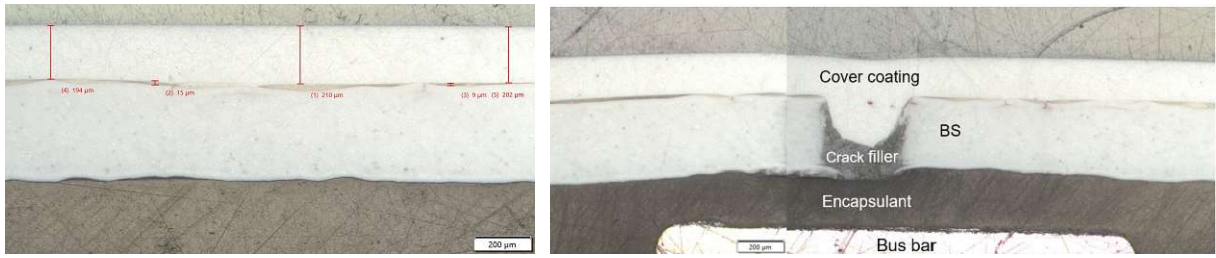
effectiveness of crack filling, as air gaps between the coating or tape layers and the BS led to total internal reflection. This phenomenon prevented the ultrasound signal from reaching deeper layers, making it impossible to assess areas with poor contact. Additionally the angled surfaces of certain cracks caused the reflected signals to deviate from the sensor's direction, further hindering a proper analysis of crack-filling extent. For this reason, SAM will not be used for crack filling analysis of the repaired full sized modules in this study.

Despite these limitations, SAM has valuable advantages. It enables clear visualization of internal interfaces, allowing identification of structural layers and defects within the BS, such as microcracks and surface irregularities, without damaging the sample. This method's non-destructive nature makes it a valuable tool for investigating PV module reliability, provided that the limitations in analyzing contact quality and thickness are taken into account.

4.2.3 Destructive Measurements

After completing the non-destructive measurements, sections of the coated BS were cut and removed from the sample module. These pieces were embedded in epoxy resin, polished, and the cross-sections subsequently analyzed using light microscopy. For future references, any mention of light microscopy of cross-sections will imply these preparation steps. In a second step, the samples were examined with ATR-IR imaging to gain further insights into the material composition and the crack filling effectiveness.

The light microscopic images of the cross-sections of the backsheet with the PU coating are shown in Figure 4.8. The image on the right reveals a successfully filled deep BS crack. However, due to the high solvent content, the crack filler exhibits significant shrinkage during the curing process, leaving the deep crack only partially filled. The much thicker cover coating compensates for this, providing an insulating layer that protects against mechanical stressors and enhances the electrical insulation of the BS. In the ATR-IR image shown in Figure 4.9 it can be confirmed that the crack filler (layer 1) was successful in filling not only the deep crack but also the much smaller micro cracks (shown on the image in the bottom right of Figure 4.9.)



(a) The Remisol coating with measured layer thicknesses of around 10 μm for the crack filler and around 200 μm for the cover coating.

(b) The two layer Remisol coating filling the deep crack of the BS.

Figure 4.8: Light microscope images of cross-sections of the coated BS.

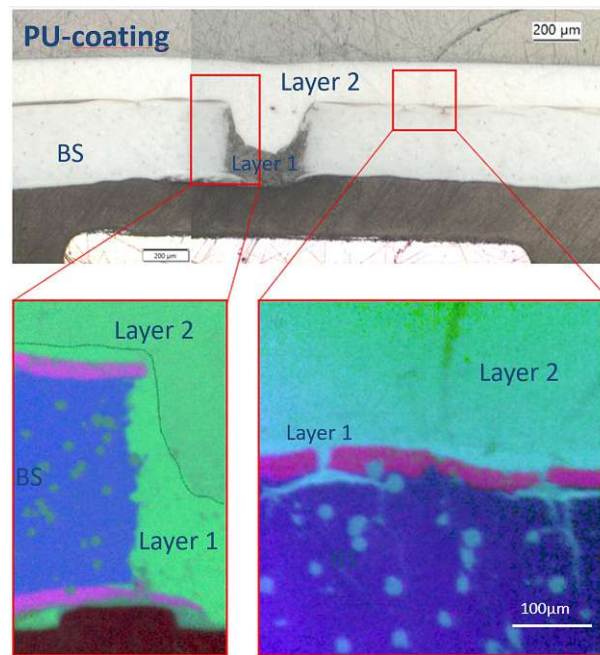


Figure 4.9: LM image (top) and ATR-IR image (bottom) of the BS coated with Remisol

In an attempt of reducing the time and labor requirement for the repair process, the crack filler was omitted to see if the cover coating alone was sufficient in filling cracks. From the results in Figure 4.10 the Cover Coating on its own seems to fill the cracks sufficiently. The shrinkage of the coating in the deep crack, however, is much more notable compared to the two layer process above.

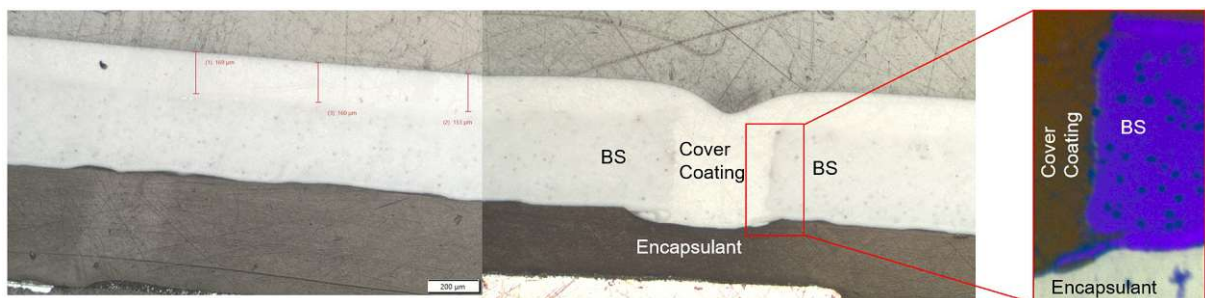


Figure 4.10: Light microscopy image and ATR-IR image of the BS coated with Remisol cover coating without the crack filler. The coating is around 160 μm thick.

In Figure 4.11 the light-microscopic images and ATR-IR-images of the cross-section taken from the BS after repair using the 3M tape are given. While the acrylic adhesive of the tape appears to successfully fill microcracks (as shown in the images on the left), the deep crack remains largely unfilled, with air occupying most of the cavity. This is attributed to the insufficient amount of adhesive present on the tape to fill the larger void.

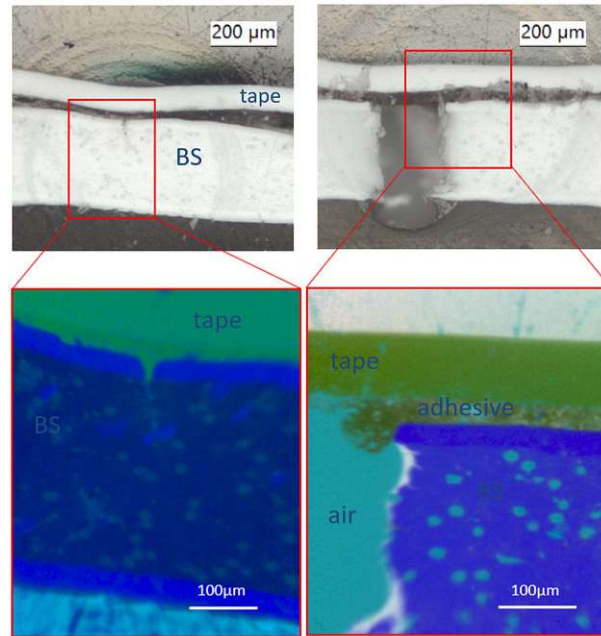


Figure 4.11: Light microscopy image and ATR-IR image of the BS repaired with tape

The silicone coating effectively filled the deep crack in the backsheet as shown in Figure 4.12. The pink coloration in the ATR-IR image on the right indicates that the silicone was able to penetrate even the smaller cavities of the torn BS without leaving air gaps. Furthermore, since silicone does not contain any solvent, no shrinkage occurs during the curing process.

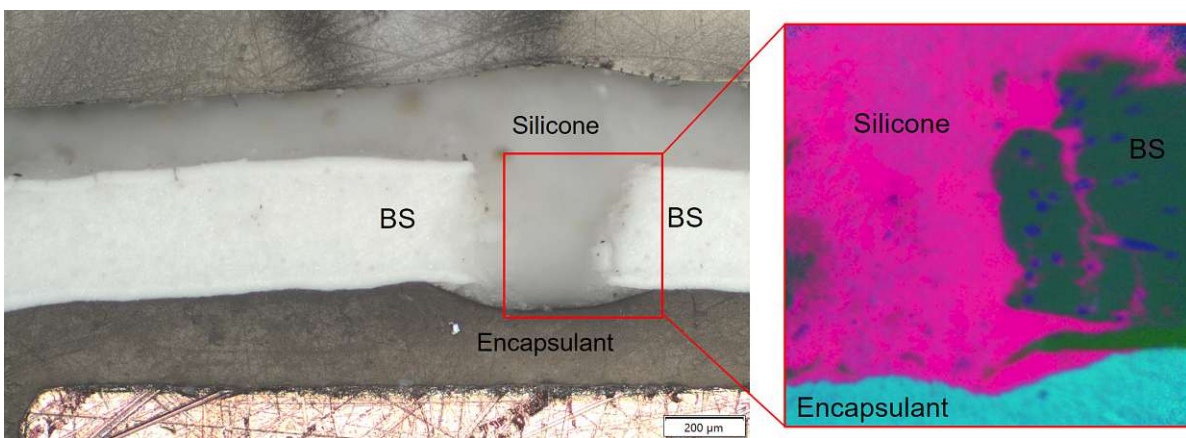


Figure 4.12: Light microscopy image and ATR-IR image of the BS coated with silicone

4.3 Main Experiment: Backsheet Repair on aged Photovoltaic Modules

This section outlines the repair process, including the characterization of the modules both before and after coating, as well as a detailed description of the coating application procedure.

Table 4.2: Overview of Repair Methods and Materials

Module	Coating	Material	Comp.	Layers	Time Requirement
M1	DOWSIL™ PV-9001 Backsheet Coating	Silicone	1	1	10 min
M2	Remisol PV Repair by Kansai-Helios	Polyurethane	2	2	15 min/layer
M3	Only Topcoat of Remisol PV Repair by Kansai-Helios	Polyurethane	2	1	20 min
M4	3M™ Wrap Foil 2080	PVC Film with Acrylic Adhesive	1	1	30 min (3 people)
M5	Uncoated (Reference)	-	-	-	-
M6	New Remisol PV Repair by Kansai-Helios	Polyurethane	2	2	15 min/layer
M7	Remisol PV Repair by Kansai-Helios	Polyurethane	2	2	15 min/layer

To calculate the amount of material required for coating one module, the following formula can be used:

$$m = \frac{\rho \cdot d \cdot A}{1 - f} \quad (4.1)$$

where:

- m is the mass of the coating,
- ρ is the density of the coating,
- d is the coating thickness, and
- A is the surface area of the BS.
- f is the mass percentage of solvent in the material

4.3.1 Silicone (DOWSi)

Using Equation 4.1, the necessary amount of silicone can be calculated. With a density of 1250 kg m^{-3} , a surface area of $0.96 \text{ m} \times 1.63 \text{ m}$, a solvent share f of 0, and a desired thickness

of $250\ \mu\text{m}$, the required mass is calculated as $0.489\ \text{kg}$. This value was rounded up by 10% to account for material losses in the container used for weighing and on the tools used to distribute the silicone.

After cleaning the BS of Module M1, silicone is pressed into the cracks as thoroughly as possible using a spatula, ensuring maximum filling of the damaged areas (see Figure 4.13).



Figure 4.13: First steps of the silicone coating process

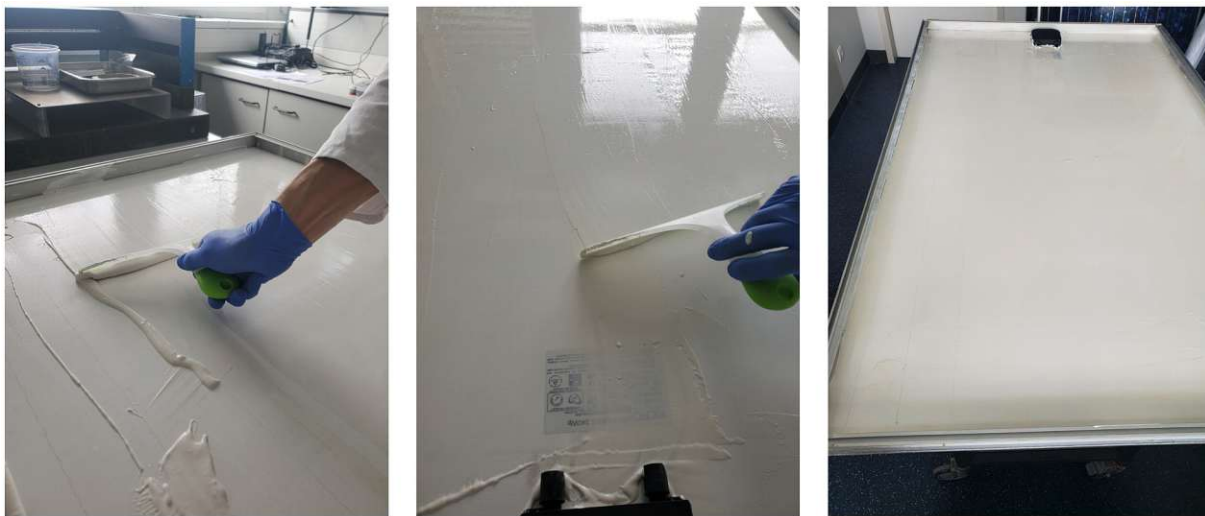


Figure 4.14: Further steps of the silicone coating process

4.3.2 Polyurethane (Remisol)

Using Equation 4.1, the necessary amounts of crack filler and cover coating for the 2K Remisol system can be calculated separately. For the crack filler, with a density of $1080\ \text{kg m}^{-3}$, a thickness of $50\ \mu\text{m}$, a solvent share of 0.398% , and the same surface area of $0.96\ \text{m} \times 1.63\ \text{m}$, the required mass is calculated as $140\ \text{g}$, excluding an additional 5% solvent to improve application and crack filling. An additional 10% was added to account for losses in coating on tools and containers. The crack filler consists of two components (prepolymer and hardener) that must be mixed in a ratio of 100A:14B, where component B is the hardener.

For the cover coating, with a density of $1415\ \text{kg m}^{-3}$ and a thickness of $200\ \mu\text{m}$, the calculated

required mass is 712 g. The two components (prepolymer and hardener) of the cover coating must be mixed in a ratio of 100A:7B, where component B is a hardener.

After cleaning the BS of Module M2, the crack filler is applied first, ensuring it is pressed thoroughly into the cracks using a spatula to maximize filling of the damaged areas (see Figure 4.15). Once the crack filler has hardened sufficiently, the cover coating is applied evenly across the surface to ensure a durable and protective layer.

For Module M3, only the Remisol cover coating was used, omitting the crack filler. This approach was intended to evaluate whether a single layer of the cover coating alone could provide comparable results in terms of crack filling and overall performance, thereby simplifying the repair process. The findings from this test will help determine the necessity of the crack filler layer in future applications.



Figure 4.15: Application of the crack filler in the Remisol coating process



Figure 4.16: Application of the cover coating in the Remisol coating process

4.3.3 Foil: PVC-Tape with acrylic adhesive (3M 1080)

The application process of the PVC foil from 3M onto Module M4 was more time-consuming than anticipated due to the difficulty of achieving a bubble-free application. The process involved three people. As shown in the right image of Figure 4.17, a few bubbles could not be avoided despite the efforts to minimize them.



Figure 4.17: Application of the 3M PVC foil

4.3.4 Wet Leakage Test

To evaluate the success of the repair process, the insulation resistance was measured in the next step.

Table 4.3 summarizes the measured insulation resistance (R_{iso}) for Modules M1 - M5 after repair. It has to be noted that all modules were also tested before coating or application of the repair film and failed in the wet leakage test (showed zero insulation resistance in wet environment). All coated modules demonstrated sufficient R_{iso} and have therefore, passed the test (see Table 4.3), meaning that they have been successfully repaired.

Table 4.3: Insulation Resistance (R_{iso}) of coated Modules from the Wet Leakage Test

Module	Coating Material	R_{iso} (M Ω)
M1	Silicone	260–300
M2	Remisol Polyurethane	300–420
M3	Remisol Polyurethane Cover Coating Only (with Hole)	250–260 (0.2)
M4	3M PVC Film	550–700
M5	Uncoated Reference Module	0.0



Figure 4.18: Test-setup for wet leakage test

After measuring a R_{iso} of only $0.2 \text{ M}\Omega$ for module M3, further investigation was conducted to identify the cause of the failure. Initially, no apparent defects were visible in the coating. However, a small hole was eventually discovered in the coating (see Figure 4.19), likely caused by a bubble or contamination during application. To address this issue, the affected area of the BS was isolated using plasticine to prevent water from reaching the hole. After this modification, the resistance improved significantly to $250 \text{ M}\Omega$ to $260 \text{ M}\Omega$. This demonstrates that even a small, barely visible defect in the coating can compromise the repair's effectiveness, leading to an unsuccessful BS restoration.

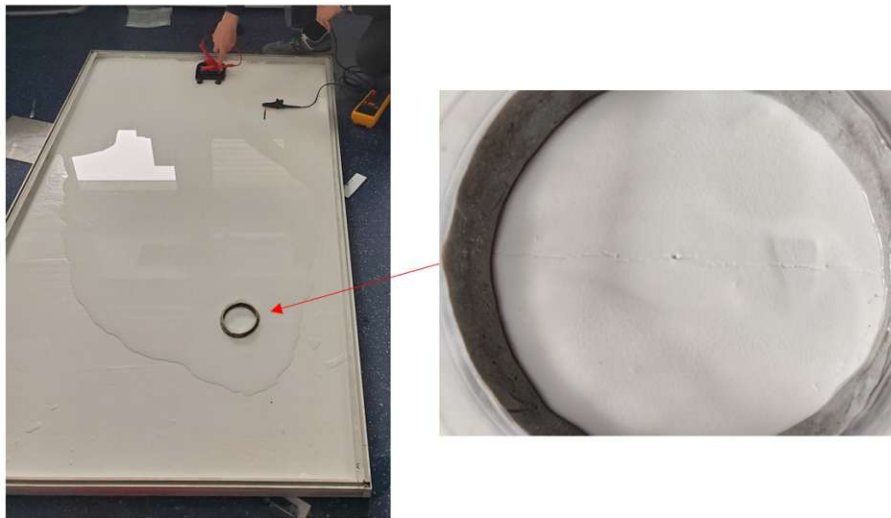


Figure 4.19: Isolation of the hole in the Remisol coating

4.4 Weathering through temperature cycles

The coated modules were subjected to weathering through temperature cycling (TC) as outlined in IEC 61215-2:2021 (MQT 11: Temperature Cycling). This test is designed to simulate the thermal stresses experienced by PV modules in real-world conditions, assessing the durability and stability of the applied coatings. Each temperature cycle consists of specific temperature and humidity changes, as detailed in Figure 4.21.

The temperature cycles started at room temperature, followed by cooling to -40°C , heating to 85°C , and then maintaining high humidity conditions (85 %) for a designated period. For the first set of 25 cycles, the test began with a cooling phase, as described in Figure 4.21. To ensure complete curing of any remaining uncured polyurethane in the coatings, the second and third sets of 25 cycles began with a heating phase, as the curing process is significantly accelerated at elevated temperatures.

The timeline of the experiment is illustrated in Figure 4.20. The process is divided into distinct stages:

- **Pre-characterization:** Initial characterization of the photovoltaic (PV) modules before the application of repair coatings.
- **Coating and curing:** Application of the repair coatings to the modules, followed by a curing period to ensure the coatings have set properly.
- **Initial evaluation:** Modules are evaluated after coating and before the start of temperature cycling (TC).
- **Temperature cycling:** The modules undergo three sets of 25 temperature cycles, simulating accelerated aging conditions. Two intermediate evaluations after 25 cycles each are being conducted.
- **Final evaluation:** A comprehensive assessment of the modules is performed after completing all 75 cycles to evaluate the long-term effectiveness of the repair methods.

This experimental setup ensures a systematic analysis of the performance and durability of the repair coatings under simulated real-world conditions.

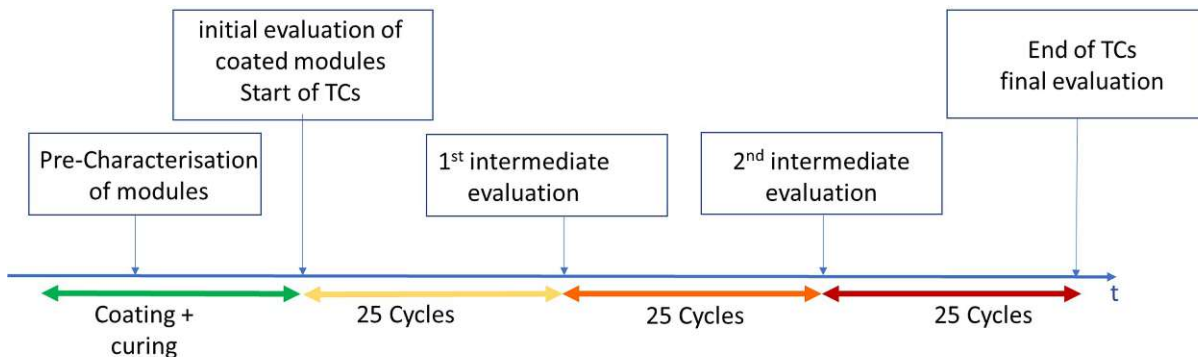


Figure 4.20: Timeline of weathering experiment

The accelerated aging test was designed to impose significant stress on the backsheets and repair coatings, ensuring a clear differentiation in performance between the tested repair materials within a short timeframe. Unlike real-world outdoor conditions, where changes in temperature and humidity occur more gradually, this test introduces rapid and extreme shifts, amplifying thermomechanical stress on the materials. As shown in Figure 4.22, the temperature cycles ranged from -40°C to 85°C , with high humidity (85 %) maintained at elevated temperatures. During the sub-zero phase, humidity measurements were not recorded due to sensor limitations, but the overall test conditions closely adhered to IEC standards.

While the accelerated test is not intended to replicate outdoor aging, it provides a more demanding scenario to observe degradation and failure mechanisms in a compressed timespan. Real-world outdoor aging, ideally conducted at a test site, would require years to reveal differences in the performance and durability of the repair solutions under test. For instance, a test site with PV modules repaired using the original PU and silicone coatings was installed more

Step	Time [min]	Temp. [°C]	rel. Humidity [%]		Temp. [°C]	rel. Humidity [%]
0	0	+25	-			
1	39	+25	-	auf	-40	-
2	60	-40	-	-	-	-
3	75	-40	-	auf	+85	85
4	120	+85	85	-	-	-
5	0	+85	85	auf	+85	0
6	36	+85	-	auf	25	0
7	60	25	25			

Figure 4.21: Figure with all temperature and humidity steps programmed for one temperature cycle

than three years ago, in the course of a research project called PVRe². This test site is well documented in the master's thesis of Anika Gassner and the coated modules have not shown any cracks in the coating or formation of new cracks in the backsheets since than [4, 16, 55, 56]. This suggests that the accelerated aging test is significantly harsher than several years of outdoor exposure, validating its utility in differentiating material performance in a controlled laboratory setting.

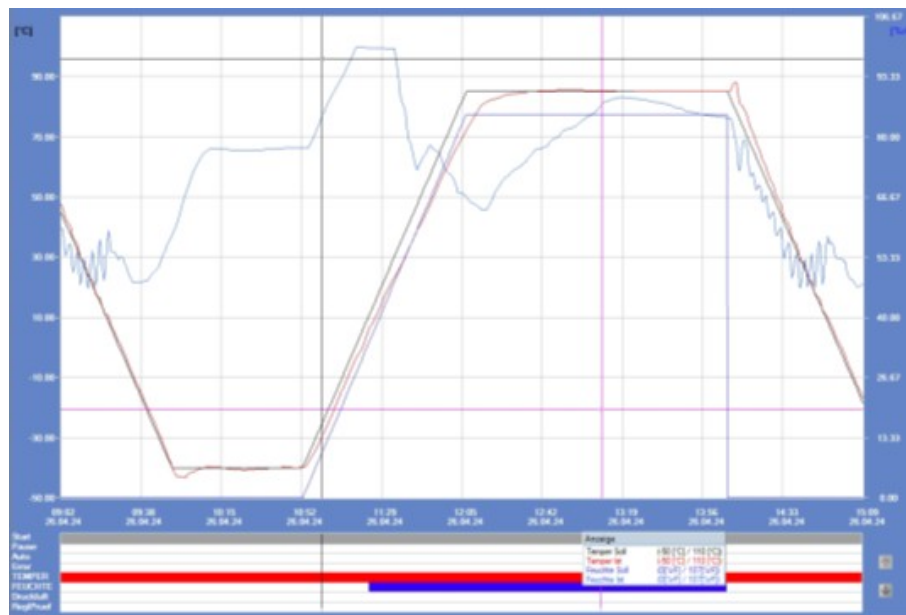


Figure 4.22: Comparison of programmed (black for temperature and dark blue for humidity) and measured (red for temperature and light blue for humidity) temperature cycles

The four coated modules (M1–M4) and the reference module (M5) were placed vertically in the climate chamber, maintaining a distance of 30 cm between each module to ensure adequate ventilation throughout the test. After the first interim evaluation modules M6 and M7 will be added (see 4.4.2).

4.4.1 Silicone Coating (M1)

During the accelerated aging tests, small cracks in the silicone coating were observed as early as 25 cycles (first interim evaluation) into the experiment (see Figure 4.23). However, these cracks did not progress significantly from one evaluation to the next. After the final evaluation, coated BS pieces of the sample module were cut out to analyze the aged coating and BS and to determine potential crack propagation. The longest cracks built after 75 cycles are shown in 4.24. As shown in the light microscope images in Figure 4.25, the cracks were limited to the surface of the silicone coating, exposing parts of the BS surface, while the deep crack remained fully filled with the coating material.

These observations align well with the results of the wet leakage test, which confirmed that the silicone-coated module (M1) passed the test. However, one critical condition for passing was that the contact between the module frame and water had to be insulated. Since this issue was not anticipated during the coating process, no particular effort was made to seal the interface between the frame and the BS. Thus, one of the key takeaways from using the silicone repair coating is the importance of ensuring a complete seal between the BS and the frame. In future applications of this repair method, special attention should be given to sealing the BS completely up to the frame to prevent potential leakage issues.

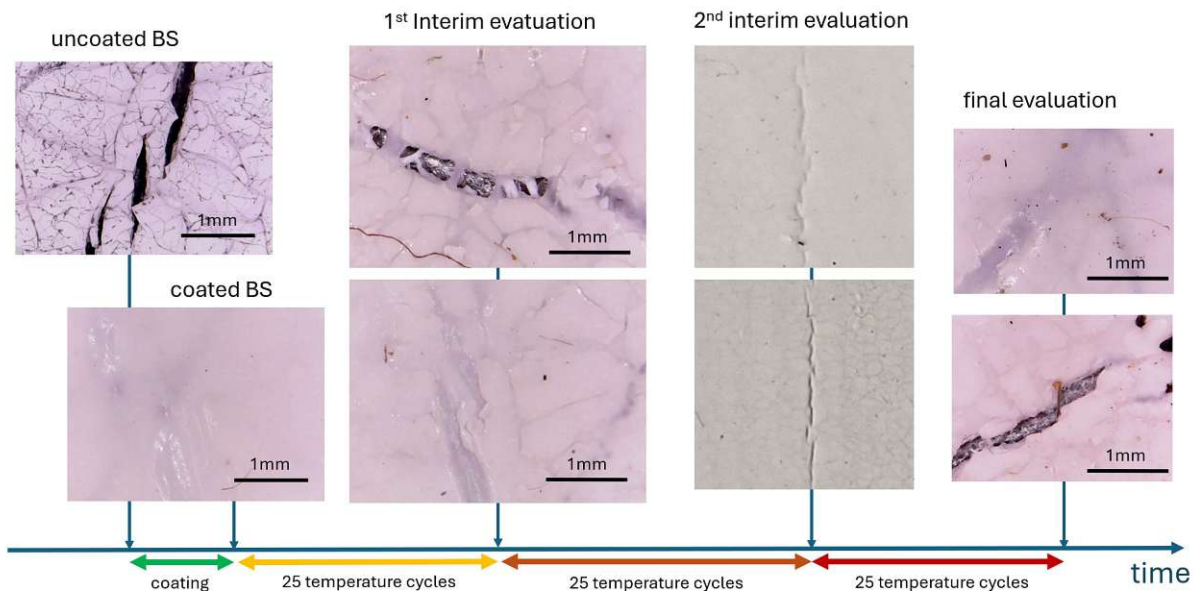


Figure 4.23: Overview of the accelerated aging results for the silicone coating on the backsheet

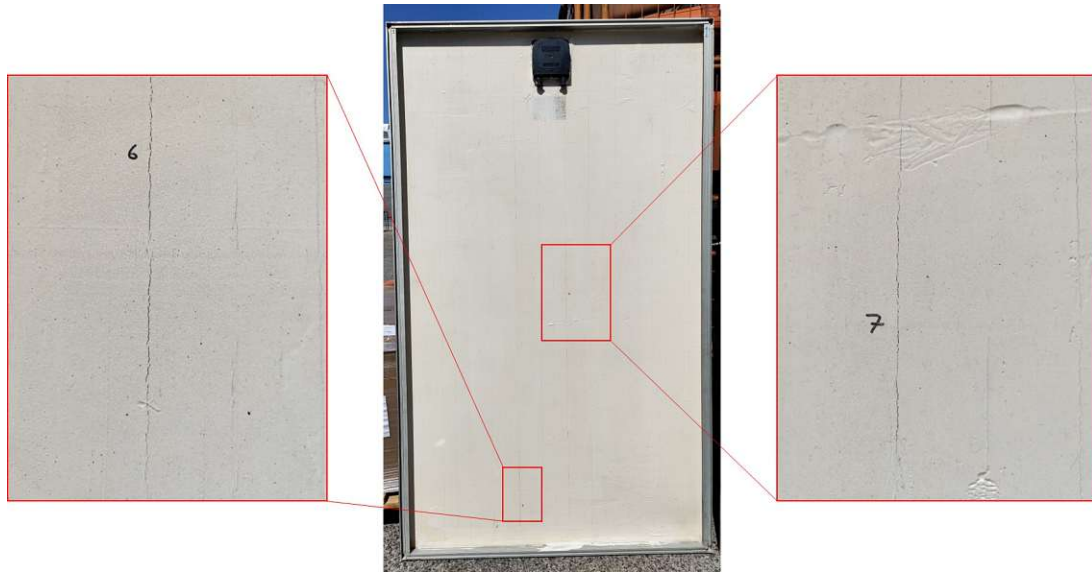


Figure 4.24: Artificially aged silicone coating showing few surface near cracks

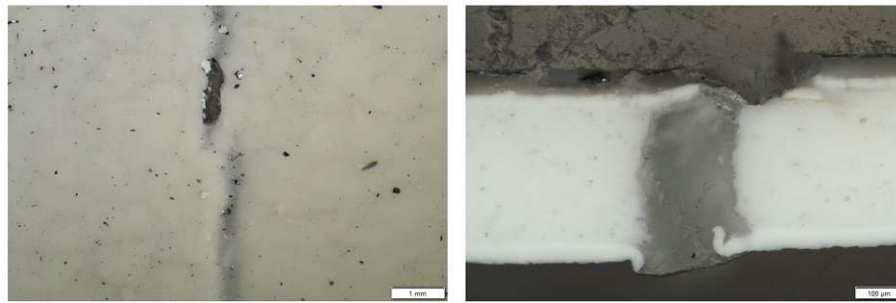


Figure 4.25: Light microscopy images of cracked coating after 75 temperature cycles

4.4.2 PU Coating (M2, M3, M6, M7)

The PU coatings, applied with two layers (crack filler and cover coating) on module 2 and one layer (only cover coating) on module 3, exhibited severe cracking after just 25 temperature cycles, as shown in Figure 4.26, 4.27, 4.28 and 4.29. Both modules (M2 and M3) failed the wet leakage test. The significantly poorer performance of these coatings compared to expectations raised questions about potential errors during the coating and curing process.

After consulting with the manufacturer, the observed issues were attributed to incomplete curing (see section 4.5) and an excessive layer thickness of the cover coating. The manufacturer recommended limiting the cover coating thickness to a maximum of 100 µm and the crack filler thickness to below 40 µm and to ensure complete curing with two days of elevated temperature at 50 °C to 60 °C.

As a result, two additional modules (M6 and M7) were coated with three key optimizations in application, material, and test parameters. In addition to the standard PU coating, a new version with a fluorine-free cover coating was applied to module M7. The optimized coating is expected to be more elastic and therefore able to withstand thermomechanical stress better caused by the backsheet during the TC.

To test the characteristics of the modified PU coating, a series of tests were conducted:

1. The absence of fluorine in this coating was confirmed through energy-dispersive X-ray spectroscopy (EDX), as shown in Figure 4.30.
2. To evaluate the elasticity and mechanical properties, as well as the material identity the

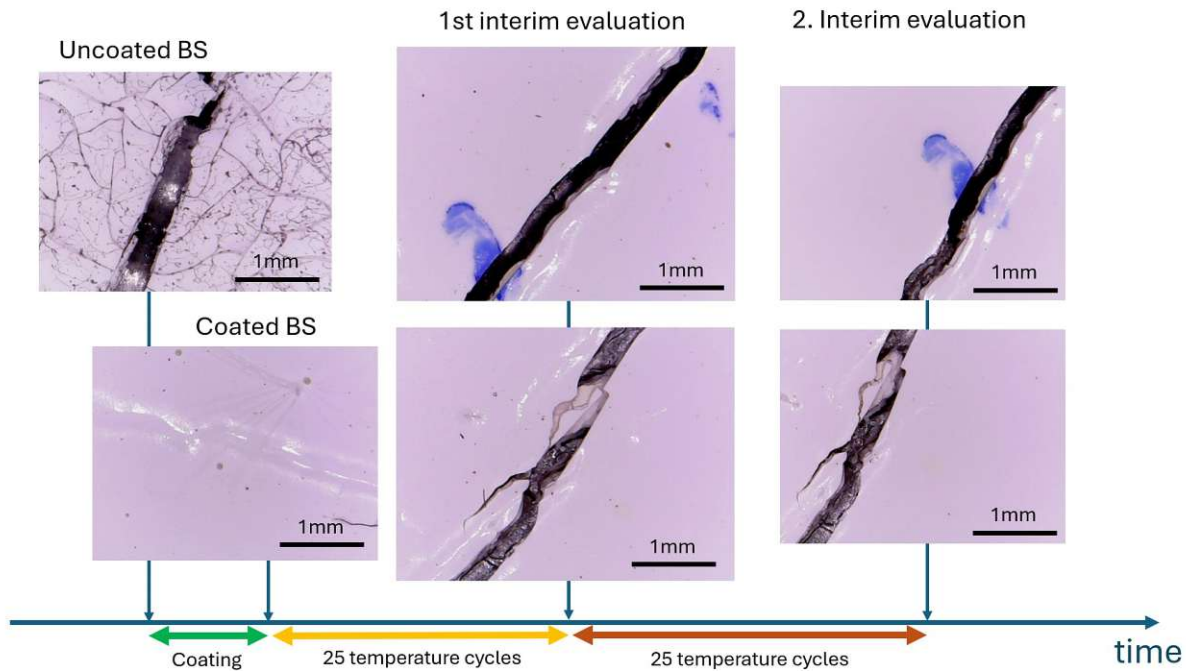


Figure 4.26: Overview of the accelerated aging results for the PU coating (Remisol) on Module M2

following tests were performed:

- (a) micro-hardness tests and nano-indentation test
- (b) tensile elongation test
- (c) IR spectroscopy analysis

Results of Micro-hardness Test 2 (a)

The micro-hardness of the modified PU coating was evaluated using the IRHD Micro-hardness method (ISO 48-2). The test was conducted on an IRHD M AA 112.031 testing device from Bareiss, with the following parameters:

- Ball Diameter: 0.4 mm
- Indentation Depth: Measured after 30 s
- Sample Thickness: Nominal thickness of 2 mm
- Edge Distance: Greater than 2 mm

The micro-hardness tests were conducted on four different coating samples: the original and optimized/new PU coatings, both in new and aged conditions. The results indicated a median IRHD M value (value between 0 (soft) and 100 (hard)) of approximately 71 for the unaged, optimized coating and around 88 for the unaged, original coating, aligning with the expected improved elastic properties of the optimized formulation. After 25 TC, the values converged to approximately 90 and 94, respectively. This suggests that the optimized PU coating maintained a relative elasticity advantage over the original formulation.

In polyurethane materials, there is a well-documented correlation between hardness and elasticity. Generally, as hardness increases, elasticity decreases and vice versa. This relationship

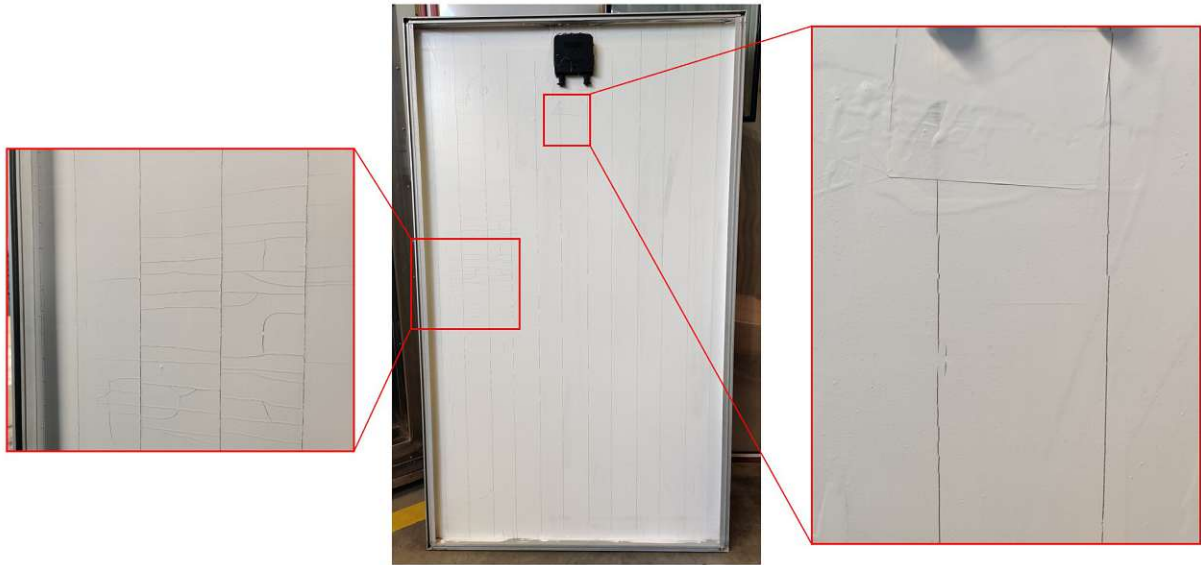


Figure 4.27: Artificially aged PU coating showing severe cracking

is influenced by the polymer's composition and structure, affecting its mechanical properties. For instance thermoplastic polyurethanes (TPUs) exhibit a range of hardness levels, with softer variants displaying higher elasticity. [40]

The results of the nano-indentation tests are illustrated in Figure 4.31, which clearly visualizes the differences between the original and optimized PU coatings. The optimized PU coating exhibits significantly softer properties, reflecting a higher elasticity (correlates to a higher indentation depth) compared to the original material.

Tensile Elongation Test 2 (b)

The tensile elongation test was conducted according to the ISO 527-3 standard using flat samples of the original and optimized PU coatings. The test was performed at a controlled temperature of 23 °C and 50 % relative humidity. A tensile testing machine (model AG-X/MST-X/X-Type, capacity 500 N) was used, and the test speed was set to 5 mm min⁻¹.

This test measures the mechanical properties of the coatings, including maximum stress (σ_{\max}), maximum elongation (ε_{\max}), and elongation at break ($\varepsilon_{\text{break}}$).

The results of the tensile elongation tests, as shown in Figure 4.32, highlight significant differences between the original and optimized PU coatings. The original coating (Figure 4.32a) shows a much higher maximum stress (σ_{\max}) but with significantly lower elongation at break (ε_{\max}). This indicates that the original coating is stiffer and more brittle, as it fails at lower elongations.

In contrast, the optimized coating (Figure 4.32b) demonstrates a lower maximum stress but much higher elongation at break. This is a clear indicator of enhanced elasticity and flexibility, making it better suited for accommodating mechanical stress and preventing crack propagation during temperature cycling or other stress-inducing conditions.

The shift in behavior suggests that the material modifications in the optimized PU cover coating effectively improved its mechanical performance by reducing brittleness and increasing its ability to stretch without failure. This improved elasticity aligns with the goal of creating a more durable and adaptable backsheet repair solution, as discussed in the context of accelerated aging tests.

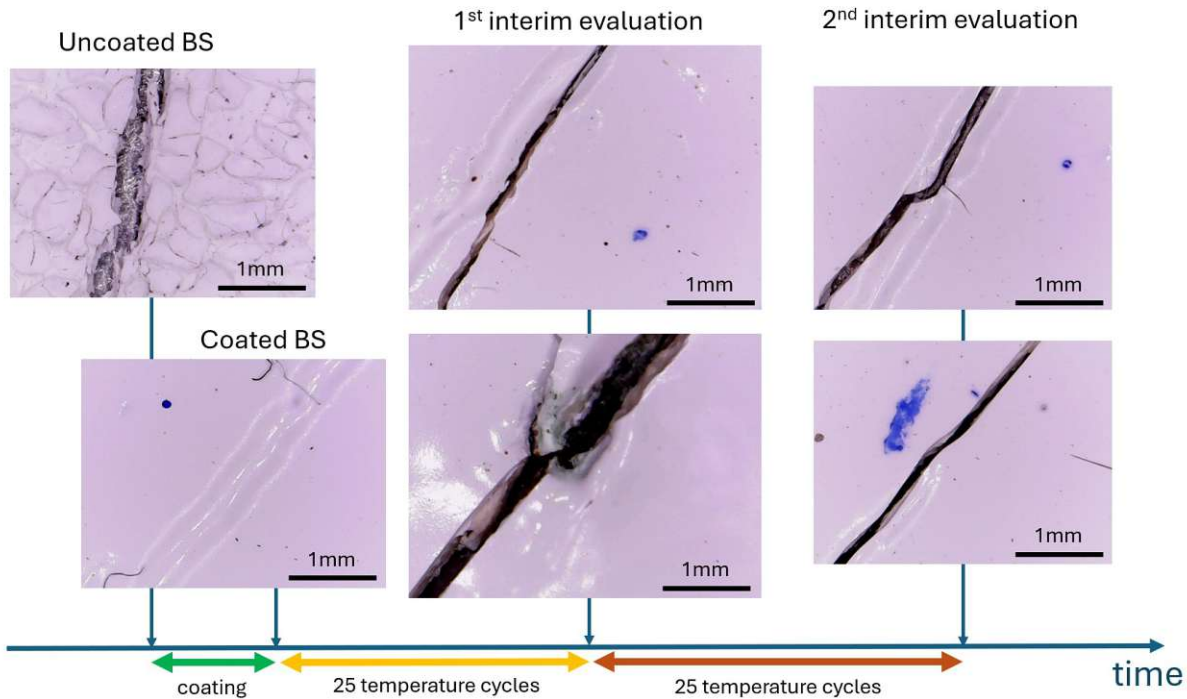


Figure 4.28: Overview of the accelerated aging results for the PU cover coating on Module M3

IR spectroscopy analysis 2 (c)

The IR spectroscopy comparison between the original and optimized Remisol coatings will be discussed in more detail in Section 4.5.

Optimized application, material and test parameters for the Remisol coating

The results of the above discussed optimizations for modules M6 and M7 are shown in Figures 4.33 and 4.34.

Even though cracks still formed and the modules did not pass the wet leakage test, there is a significant improvement compared to the results before the optimization. The cracks now appear only above the existing backsheet cracks, clearly indicating that they are caused by the thermo-induced movement of the backsheet. A metal plate also coated with the original and optimized PU coatings, which also underwent the TC for comparison, showed no cracks in the coating, supporting this claim. The only exception is a delamination of the coating, as documented in the bottom left of Figure 4.33.

These results demonstrate that the optimizations have clearly improved the outcome of the experiment. Although the ideal result of achieving repaired modules that pass the wet leakage test was not achieved, the primary goal of showing a measurable improvement has been successfully obtained.

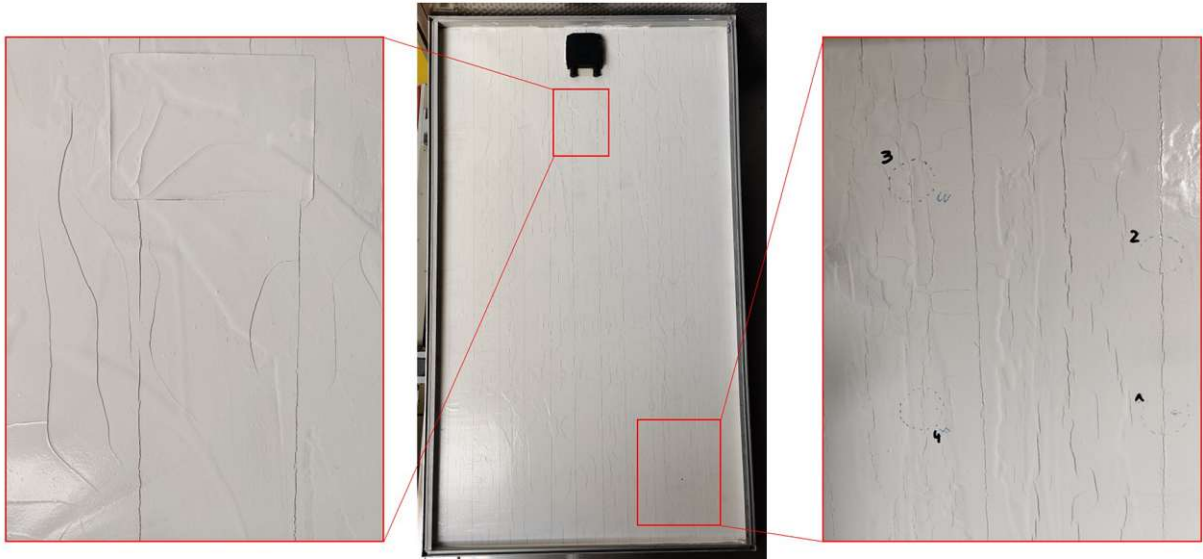


Figure 4.29: Artificially aged PU coating showing severe cracking

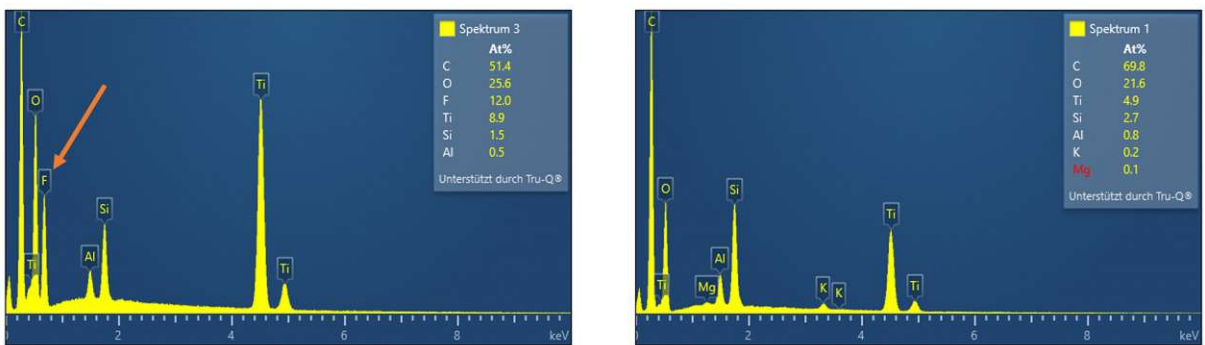


Figure 4.30: Comparison of the Energy-dispersive X-ray spectroscopy results of the original (left) and the new (right) PU cover coating

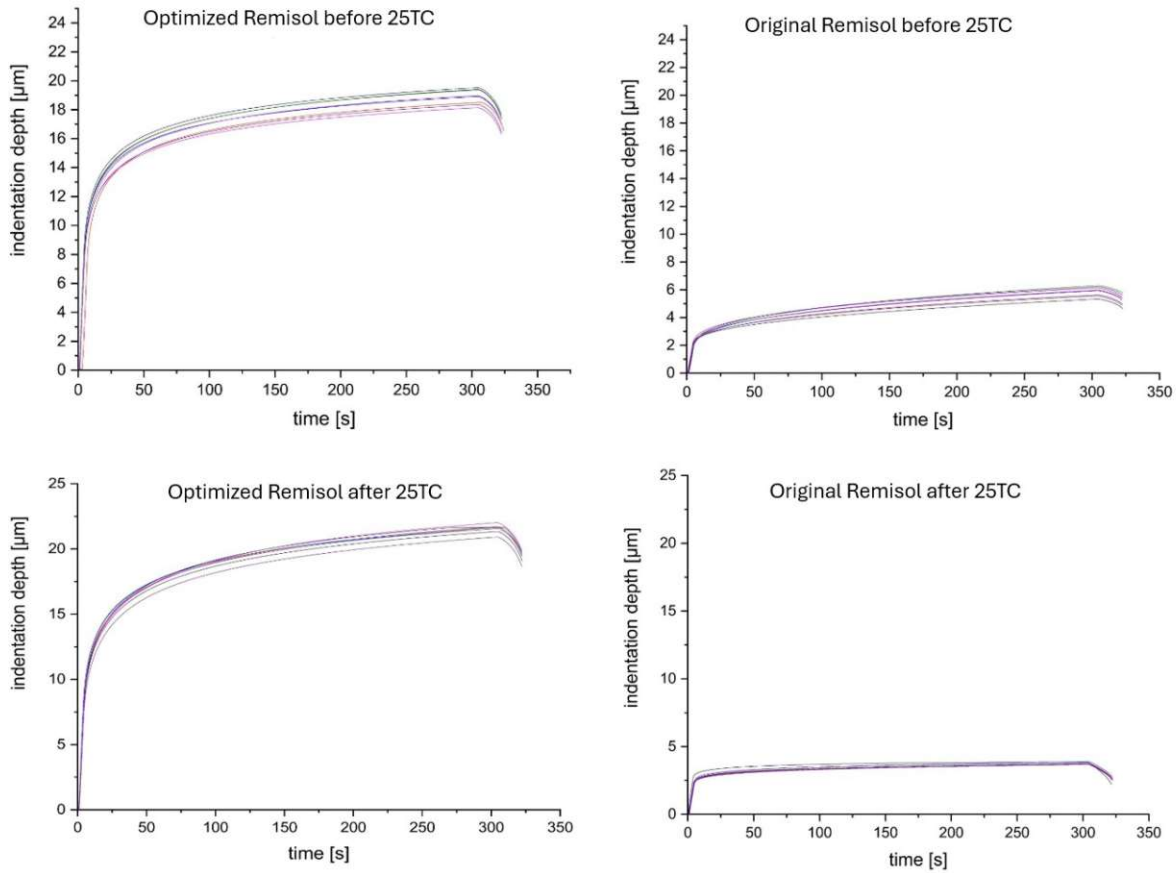
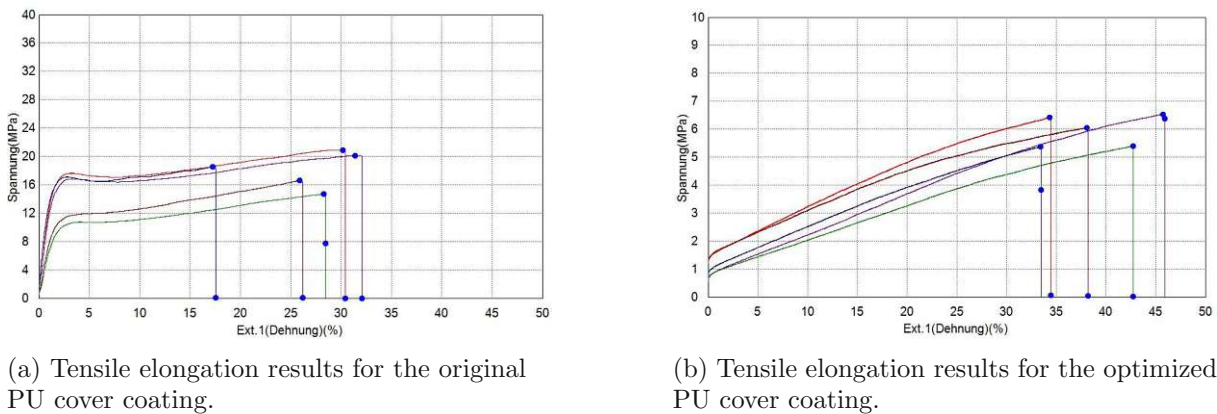


Figure 4.31: The nano-indentation results for the the PU coating before and after 25 TC



(a) Tensile elongation results for the original PU cover coating. (b) Tensile elongation results for the optimized PU cover coating.

Figure 4.32: Comparison of tensile elongation test results for the original and optimized PU coatings. The diagrams illustrate differences in stress (σ_{max}) and elongation (ϵ_{max}) between the two coatings, highlighting the enhanced elasticity (corresponds to higher elongation at break) of the optimized coating.

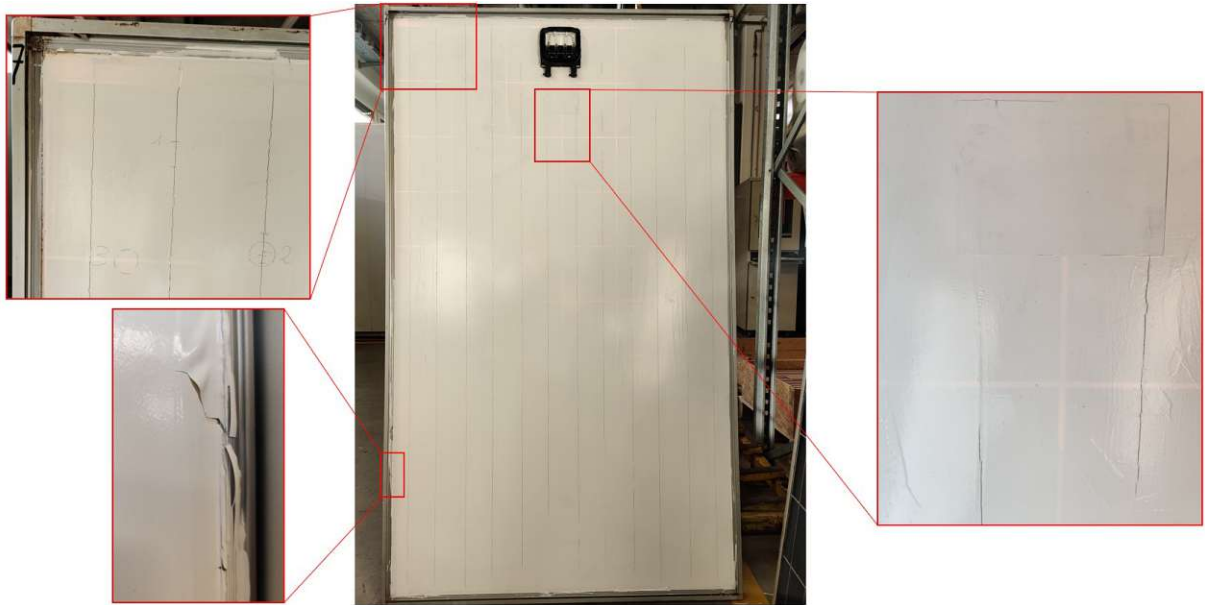


Figure 4.33: The original PU coating on Module M7 after 25 TC with the modified application and test parameters



Figure 4.34: The optimized PU coating on Module M6 after 25 TC with the modified application and test parameters

4.4.3 Tape (M4)

While remaining largely intact during the first 25 temperature cycles, the sample module M4 with the 3M Wrap Tape 1080 adhered to the backside began to show signs of tearing after 50 cycles, with more extensive damage observed after 75 cycles (see Figure 4.35). The module M4 passed the wet leakage test after 25 and 50 cycles but failed the test after 75 cycles. As shown in Figure 4.36, the tape shrank over time, exposing the BS surface near the frame.

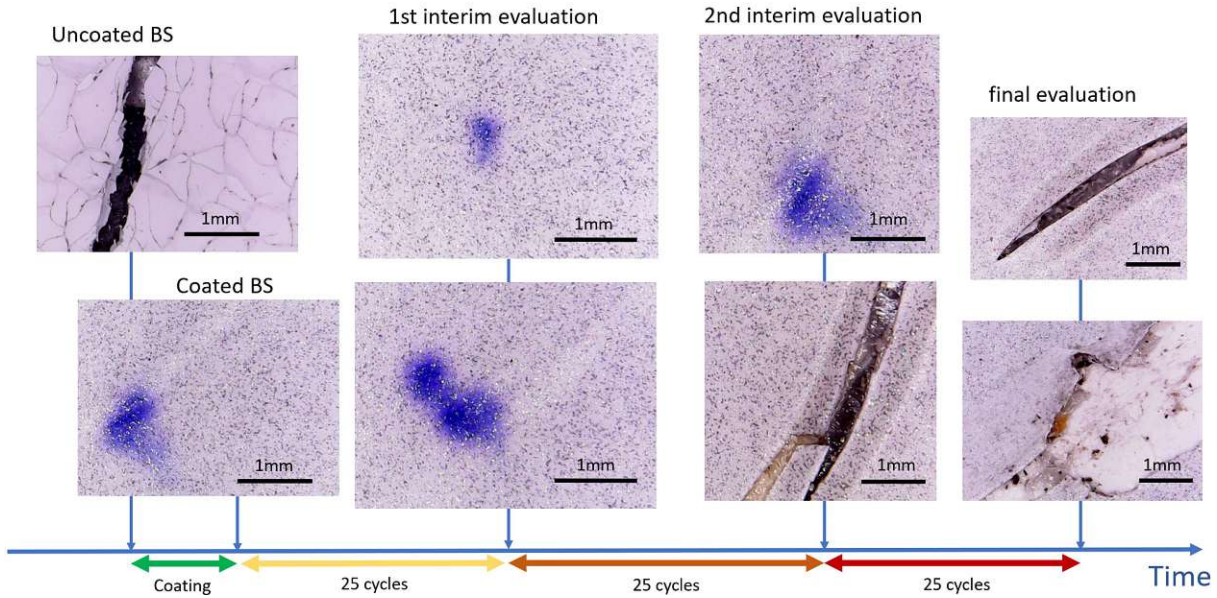


Figure 4.35: Overview of the accelerated aging results for the 3M Wrap Tape (The blue spots are color markings and not caused by or linked to degradation)



Figure 4.36: Ripped Tape after 75 cycles

4.4.4 Uncoated Reference Module (M5)

While it is more challenging to observe the degradation of the module's BS in the microscopy images shown in Figure 4.37, the damage becomes evident in Figures 4.38 and 4.39. Increasing numbers of deep cracks have formed, not only above the bus bars but also in other areas of the BS, running parallel to the bus bars and existing cracks. Additionally, progressive yellowing of the BS can be observed, with the effect being most pronounced in the right image of Figure 4.39.

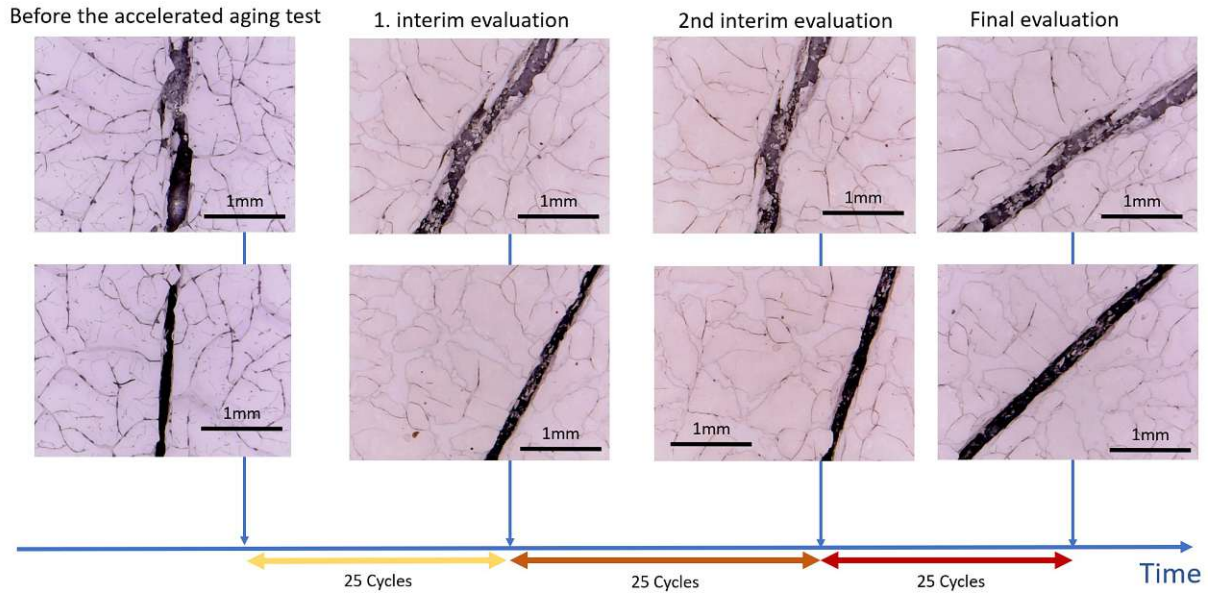


Figure 4.37: Overview of the accelerated aging results for the uncoated reference module

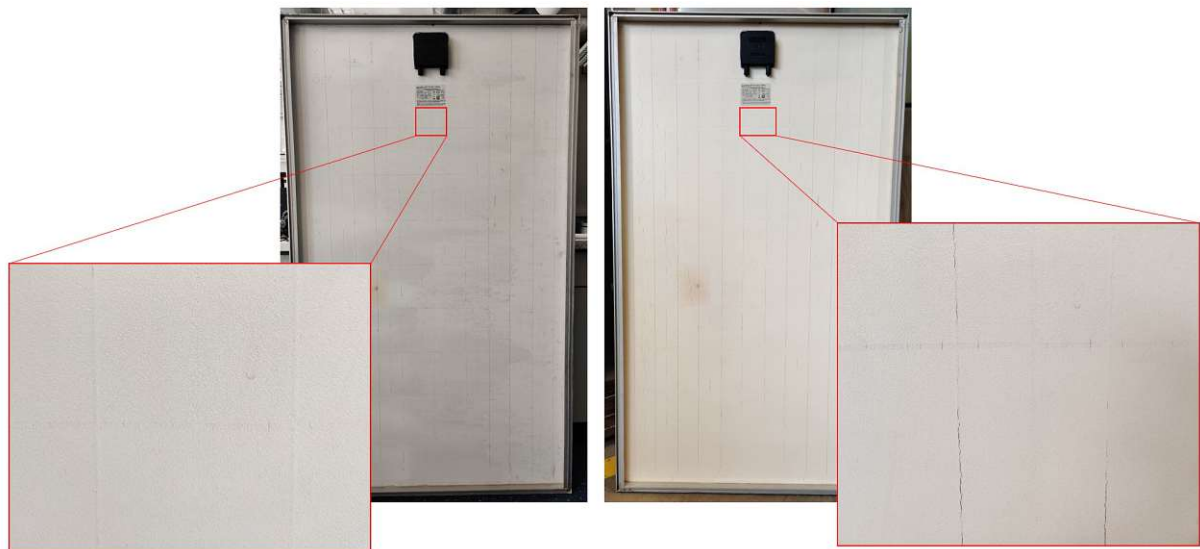


Figure 4.38: Comparison between uncoated reference module before and after 25 temperature cycles

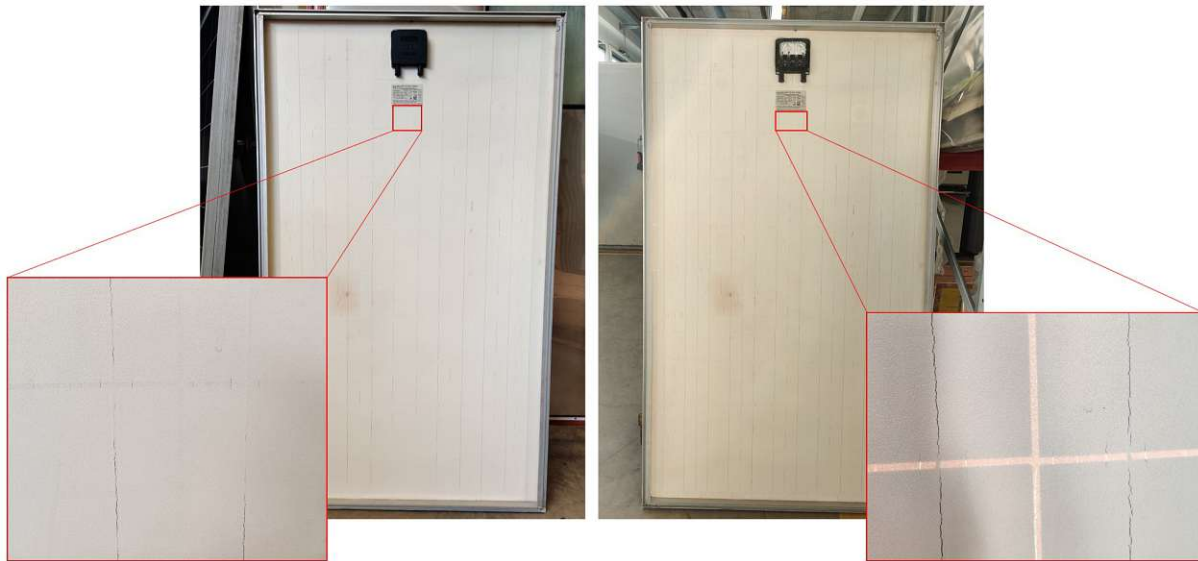


Figure 4.39: Comparison between uncoated reference module after 50 and 75 temperature cycles

4.5 IR Spectroscopy

IR spectroscopy was employed to detect potential chemical changes on the surface of the backsheet. This technique provides insights into the molecular structure and possible degradation processes. Measurements were taken after completing the repair process to establish a baseline and were repeated after the temperature cycling tests to assess any chemical alterations induced by aging. This approach allowed for a comparison of the surface's chemical stability under accelerated aging conditions.

The uncoated reference module M5

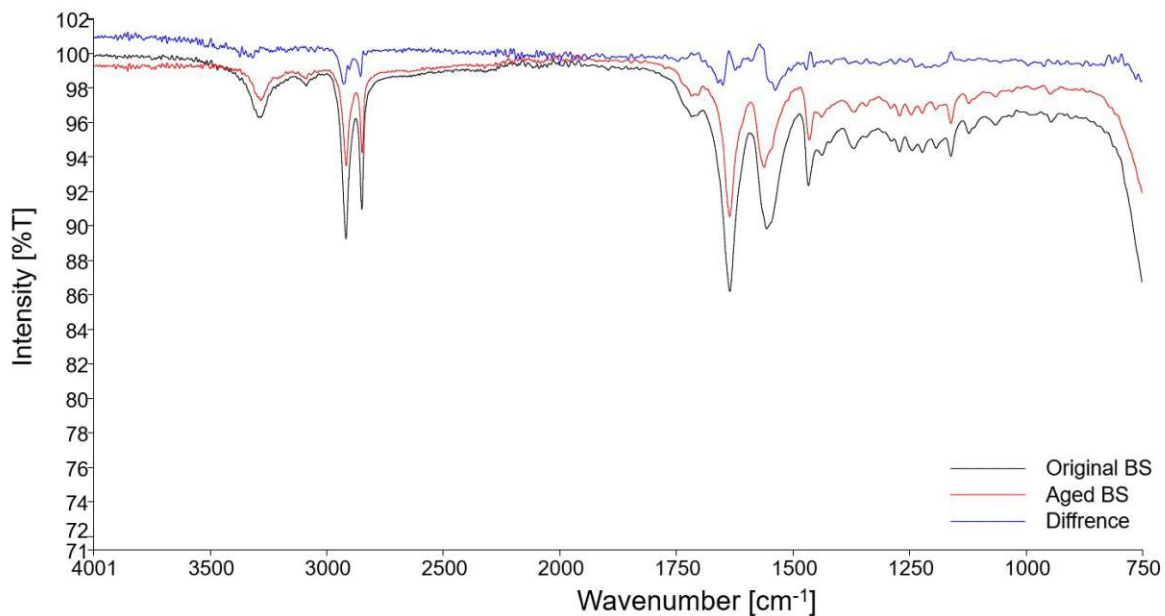


Figure 4.40: Comparison between IR spectra of the backsheet of the uncoated reference module before and after the 75 temperature cycles

In Figure 4.40 the IR spectra of the original backsheet (BS) and the aged backsheet are compared and the difference spectrum (blue) included. The difference spectrum in this section will always be a subtraction of the aged from the original sample. Key observations are as follows:

The N-H stretching vibration at approximately 3300 cm^{-1} remains unchanged, as indicated by the flat baseline in the difference spectrum. This observation confirms that no significant structural changes have occurred in the amide bonds.

A slight shift is detected in the CH stretching vibration at 2880 cm^{-1} to 2900 cm^{-1} . However, the magnitude of this shift is minimal and does not indicate chemical degradation.

The carbonyl (C=O) band at 1700 cm^{-1} to 1740 cm^{-1} is present, suggesting that oxidative damage had occurred prior to the temperature cycling. This band would not have been observed in an undamaged sample. However, no notable changes in intensity or position were detected after the cycles, confirming that no further oxidation took place during the experiment.

The polyamide 1 and 2 bands, located at approximately 1640 cm^{-1} and 1554 cm^{-1} , exhibit a slight shift. This shift may indicate a polymer rearrangement or surface-level changes rather than bulk degradation, as the ATR-IR method used for measuring the spectra only penetrates the material to a depth of a few micrometers.

Finally, no additional peaks corresponding to carboxylic acid or hydroxyl groups are observed, confirming that no hydrolysis has taken place.

Overall, the analysis confirms that the backsheet maintained its structural integrity, with no evidence of chemical degradation, such as oxidation or hydrolysis, observed during the accelerated aging tests. The only notable changes were minor surface modifications, as indicated by subtle shifts in the polyamide peaks, which do not suggest significant deterioration.

The Silicone Coating

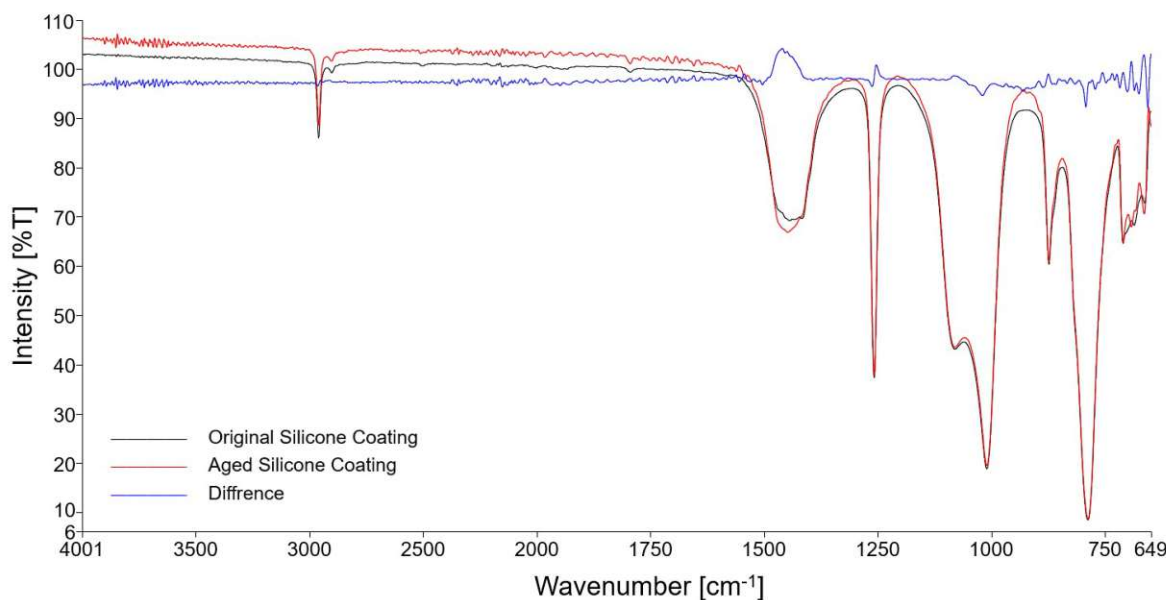


Figure 4.41: Comparison of the IR spectra of the silicone coating before and after the 75 temperature cycles

The silicone coating shows minimal changes in the IR spectrum in Figure 4.41 after aging, as expected from the stable chemical properties of silicone. The observed differences can be attributed to chalk (see 4.42) residues on the aged surface, likely caused by evaporating water

during the temperature cycles in the climate chamber. These residues are superficial and do not indicate chemical degradation of the silicone material itself.

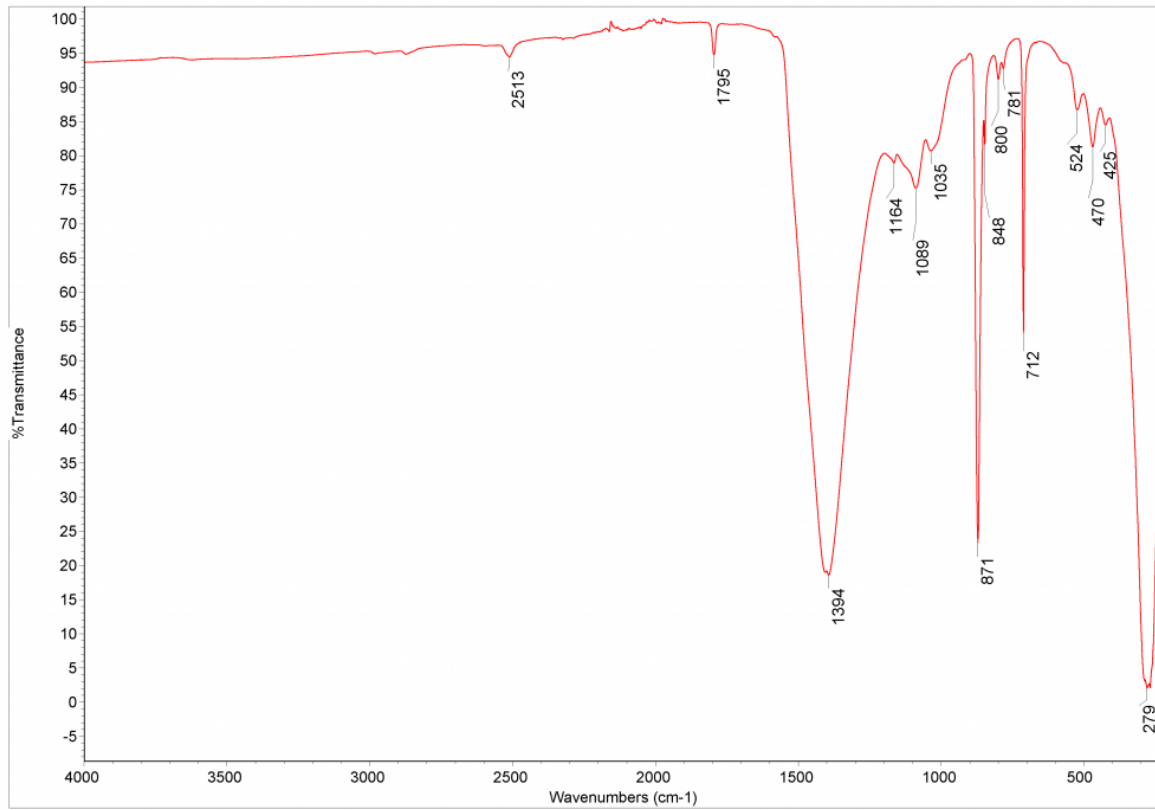


Figure 4.42: The IR spectra of chalk from [54]

The PVC Foil

The IR spectrum of the 3M PVC foil does not represent a pure PVC signal due to the presence of a methacrylate-based color coating on its surface, which was also captured in the IR measurement. After the accelerated aging process, the spectrum remains largely unchanged. However, slight variations in the CH bands at 2880 cm^{-1} to 2900 cm^{-1} were observed, suggesting minor changes limited to the surface layer of the foil. This behavior is illustrated in Figure 4.43.

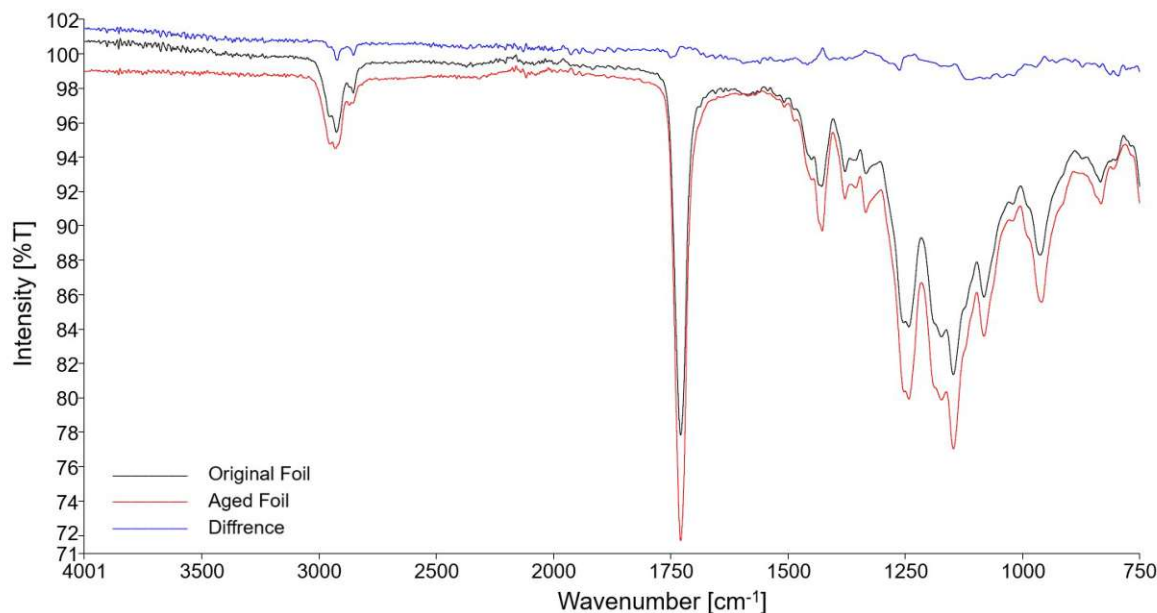


Figure 4.43: Comparison between the IR spectra of the 3M PVC Foil before and after the 75 temperature cycles

The PU Coating

The IR spectra of the PU coating before and after TC, shown in Figure 4.44, exhibit a small change in the carbonyl peaks after aging. Furthermore, in the spectrum of the original coating, it is visible that not all of the isocyanate component (2270 cm^{-1}) of the polyurethane had reacted, indicating that the curing reaction was incomplete. The manufacturer confirmed that the surplus of the isocyanate component is intentional, serving a hygroscopic function. This excess isocyanate reacts with any residual moisture within the crack, ensuring that no water remains trapped beneath the coating. This incomplete curing could be a significant factor contributing to the high number of cracks observed after just 25 temperature cycles, as discussed in Section 4.4.2.

The new peaks appear in the IR spectrum of the optimized PU cover coating shown in red in Figure 4.45 at approximately 3100 cm^{-1} , corresponding to aromatic C–H stretching vibrations and in 1500 cm^{-1} and 1600 cm^{-1} corresponding to C=C bending vibrations possibly from an aromatic ring [32]. These peaks indicate the presence of aromatic structures in the material, likely resulting from a styrenization process. Additionally, the disappearance of the isocyanate peak at 2270 cm^{-1} confirms that the curing reaction has been fully completed.

Figure 4.46 demonstrates that the coating did not undergo significant chemical degradation. Only minor changes in the carbonyl peaks and the C–H peaks can be observed.

The IR spectroscopy results confirm that all repair materials and backsheets maintained their chemical integrity during the accelerated aging tests. Minor surface-level changes, such as shifts in CH and carbonyl peaks, were observed in some cases but did not indicate significant

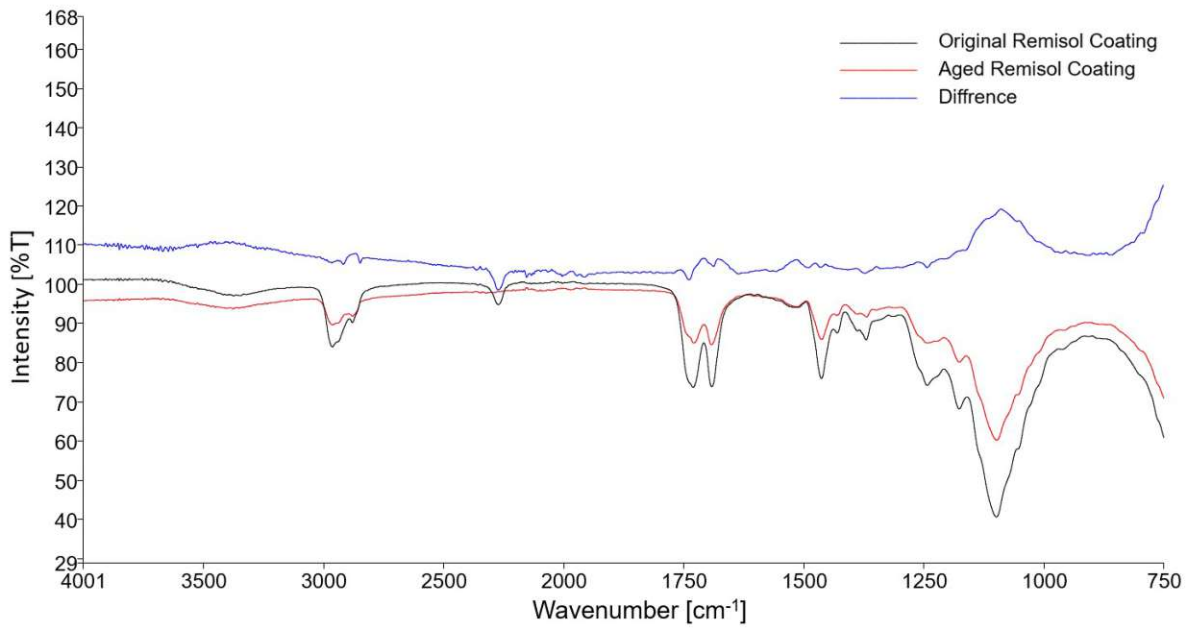


Figure 4.44: Comparison of the IR spectra of the Remisol coating before and after 50 temperature cycles

degradation. These findings highlight the chemical stability of the repair coatings and their potential to extend module lifetimes under realistic operating conditions.

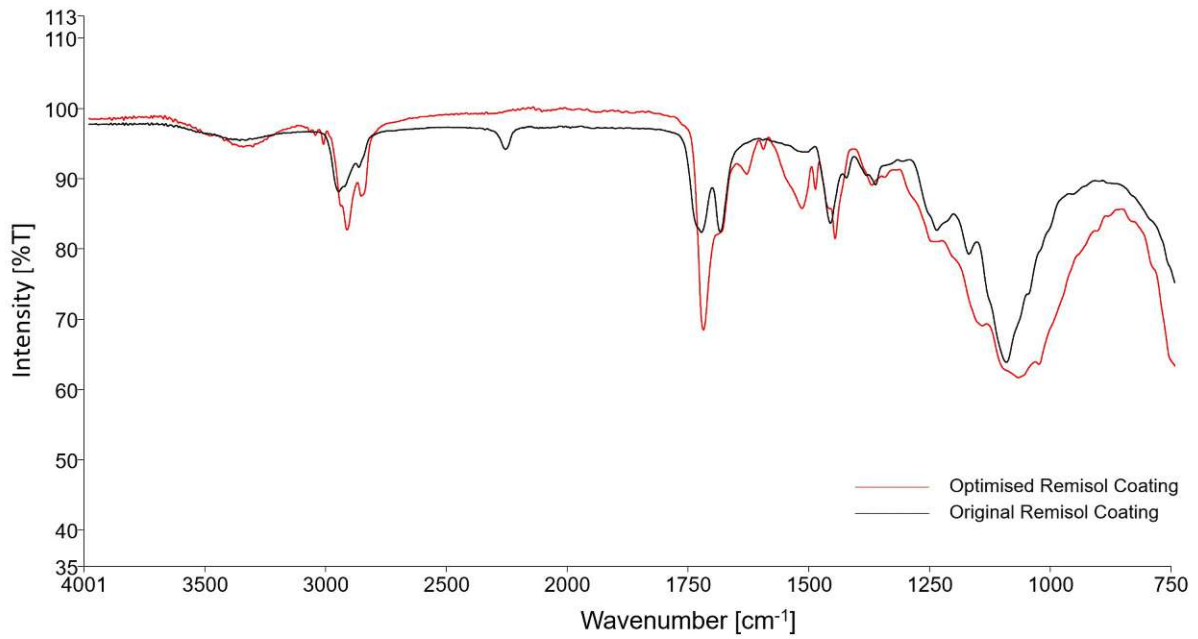


Figure 4.45: Comparison of the IR spectra of the original and the optimized PU cover coating (before the accelerated aging test)

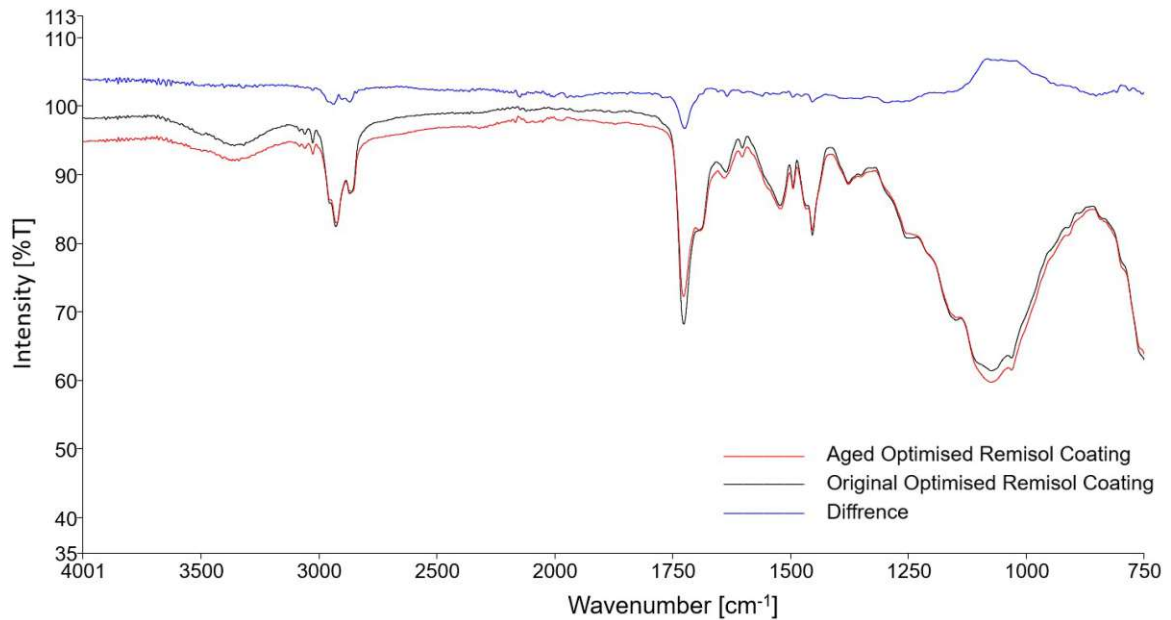


Figure 4.46: Comparison of the IR spectra of the optimized PU cover coating before and after 25 temperature cycles

4.6 Performance measurements

The maximum power output of the modules was measured using the I-V-400w device from HT Instruments, as described in Section 3.3.1. To ensure accurate calculations for the maximum power at standard test conditions (STC), the irradiance should be not lower than 800 W m^{-2} , and the cell temperature should not deviate too much from 25°C .

In Figure 4.47 and Table 4.4, a comparison of the measured electrical performance results before and after the accelerated aging test is shown. Due to the already significant variation in maximum power (P_{\max}) before the test, it is challenging to compare the degradation between the coatings and the reference module. This difficulty arises because the degradation rate is not linear and dependent on many factors such as temperature cycles and mechanical stress, and modules with a higher initial degradation tend to exhibit an accelerated degradation rate.

Table 4.4: P_{\max} comparison before and after the accelerated aging test.

Module	P_{\max} before	P_{\max} after	Power Degradation
M1	227W	198W	-13%
M2	235W	195W	-17%
M3	225W	218W	-3%
M4	230W	187W	-19%
M5	190W	140W	-26%

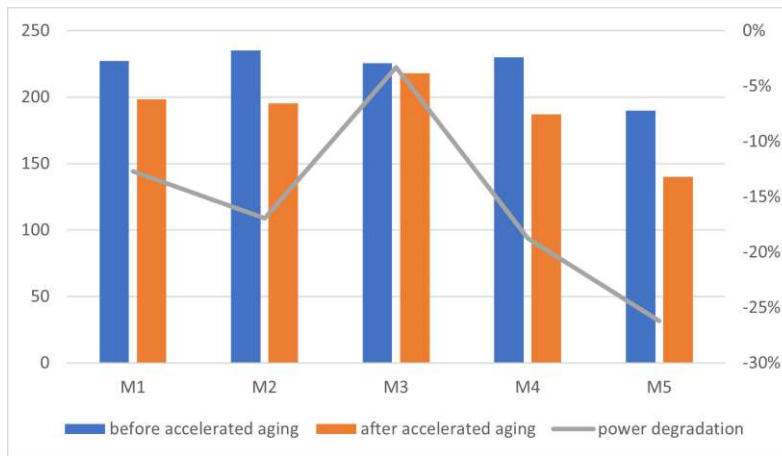


Figure 4.47: Calculated P_{\max} for standard conditions before and after the temperature cycles and the power degradation in percent. The modules are rated for a peak power of 240 W

4.7 Electroluminescence measurements

Electroluminescence (EL) measurements were conducted using a camera sensitive to infrared light in the wavelength range of 900 nm to 1100 nm. The measurements were performed in a dark room both before and after the temperature cycling test. The dark room was chosen to reduce visible and infrared light from the environment. The primary goal was to assess whether the cells sustained any damage during the aging process and to compare the coated modules (M1–M4) with the uncoated reference module (M5).

Figure 4.48 illustrates how the TC process resulted in significant cell degradation, primarily in the form of cell cracks. A healthy cell emits an evenly distributed amount of light across its surface, which is noticeably disrupted in the damaged cells. Among all modules, the middle string consistently appears to be the most intact. While the relatively intact strings in all

modules developed a comparable number of cracks, it is particularly striking that the middle string of module M5 exhibited a much higher level of degradation, forming numerous cracks. This level of degradation was significantly higher than in the coated modules, despite M5 starting with a similar pre-TC condition.

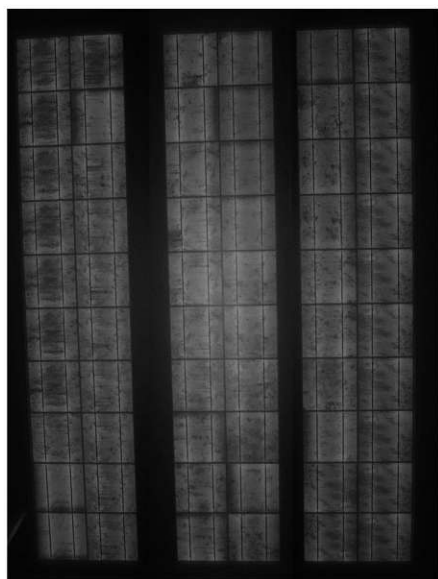
It is important to note that the TC process is specifically designed to accelerate aging and highlight vulnerabilities in PV modules, including cell cracking and other cell-related defects. The results shown in Figure 4.48 align with this purpose, as the cycling induces stress that exacerbates pre-existing defects and highlights areas prone to failure under extreme conditions.

The images in Figure 4.48 appear unconventional due to the methodology used for electroluminescence (EL) imaging. Each string was measured separately because of the lack of a sufficiently strong power source to illuminate all strings simultaneously. This is why each module consists of three images that have been patched together, therefore leaving a black bar between the strings that is wider than the gap between cells in the module.

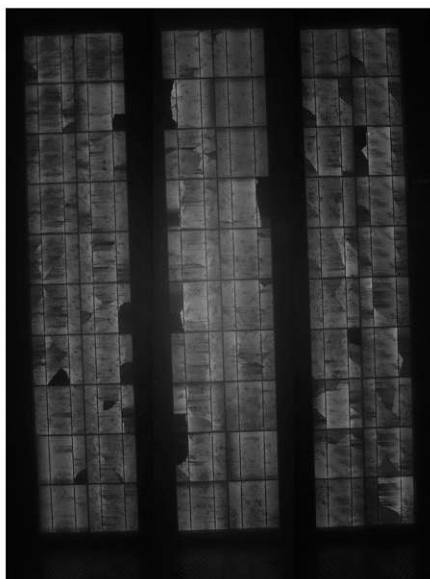
It should also be emphasized that while the observed degradation is notable, these images do not provide direct evidence of whether one coating performed better or worse in preventing cell degradation. At most, the data may suggest correlations, but no causative conclusions can be drawn from these images alone. Further quantitative analysis and systematic comparisons are required to assess the relative effectiveness of the coatings.

4.8 Conclusion

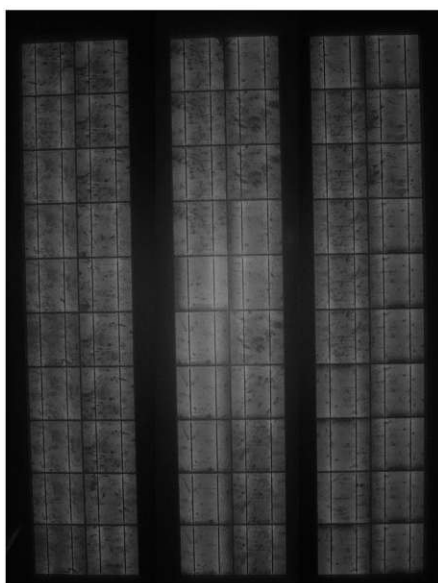
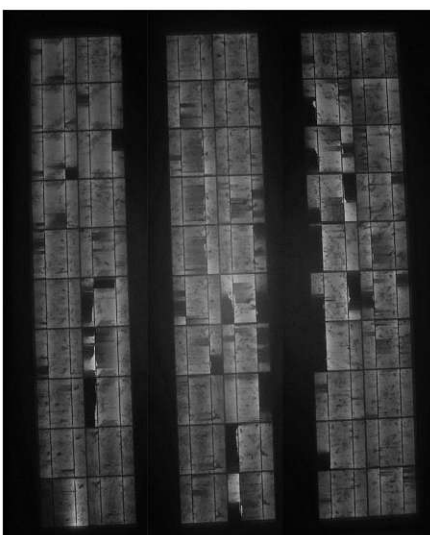
In conclusion, the experiments demonstrated that while all repair materials initially improved the insulation behavior of the backsheet under wet conditions, their long-term stability varied under thermal cycling. Silicone maintained its insulating properties when properly applied, whereas polyurethane coatings required further modifications to prevent cracking. Tape-based repairs showed early signs of delamination and shrinkage, limiting their effectiveness for deep cracks.



(a) Module M1

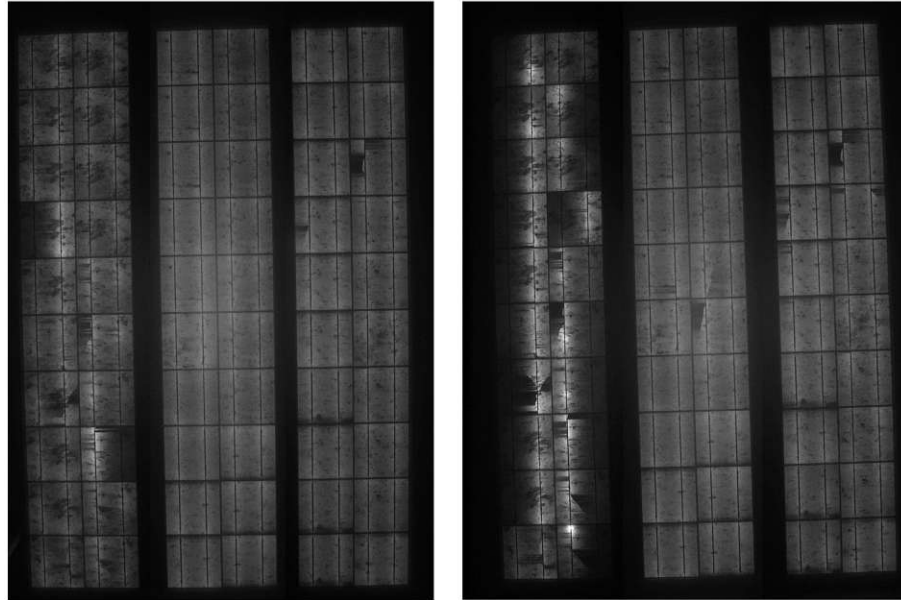


(b) Module M2

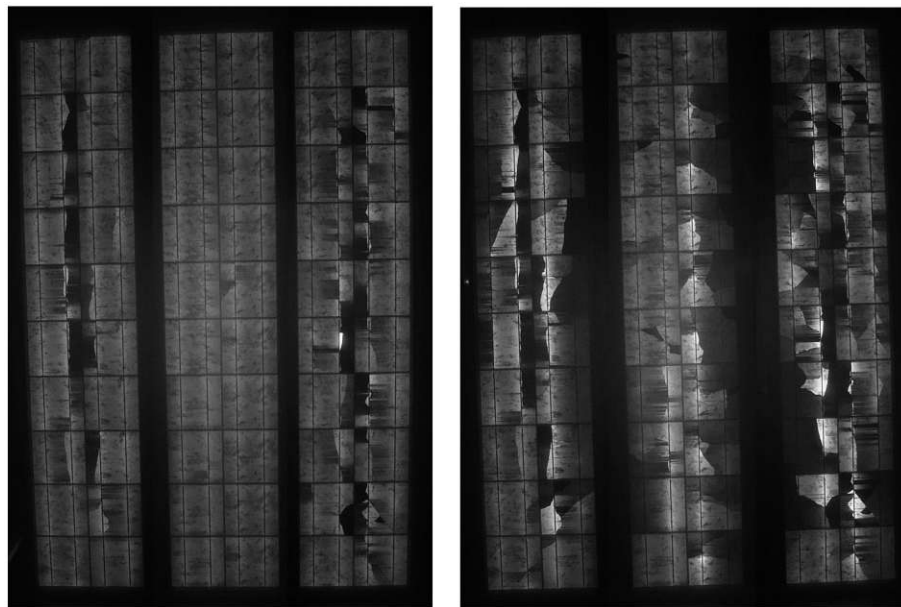


(c) Module M3





(d) Module M4



(e) Module M5

Figure 4.48: Comparison of EL images of modules M1–M5 before and after the 75 TC aging process.

Chapter 5

Discussion

This chapter critically evaluates the findings of this study, addressing the research questions through an analysis of the repair methods' effectiveness, their implications, and their potential applications in photovoltaic module maintenance. Additionally, the extension of the operational lifetime of repaired modules contributes to improved life cycle assessment metrics, highlighting the environmental benefits of effective backsheet repair strategies.

5.1 What is the most reliable method for examining the crack-filling effectiveness of repair coatings?

The most reliable quantitative method for evaluating the crack-filling effectiveness of repair coatings was ATR-IR imaging combined with light microscopy of cross-sections. These destructive techniques provided precise insights into the degree of crack filling and the presence of air gaps. By enabling direct visualization and material characterization, these methods offered critical data to confirm the effectiveness of the applied repair materials.

Non-destructive methods, such as Scanning Acoustic Microscopy (SAM), were less effective in this context due to being unable to visualize microcracks and detecting gaps in angled or deep cracks. While SAM remains valuable for initial assessments and structural analysis, its inability to accurately measure filling effectiveness for deep or angled cracks limits its utility for this application.

5.2 How do the applied coatings perform under accelerated aging conditions?

The accelerated aging tests revealed significant differences in the performance of the repaired coatings and tapes tested. Silicone demonstrated superior durability, with only small surface cracks formed but no significant degradation of its crack-filling capability. These results align with the wet leakage test, where the silicone coated module passed with proper application to the frame edges.

The original PU coating cracked severely after just 25 temperature cycles. After optimizing the material composition, application process, and curing parameters, the performance improved markedly. Cracks were limited to areas directly above the backsheet cracks, indicating better adhesion and flexibility. Despite these improvements, the modules with optimized coatings

passed the wet leakage test after coating but still failed the test after 25 TC, underscoring the need for further optimization.

The PVC tape with acrylic adhesive exhibited delamination and shrinkage over time in the climate chamber, resulting in failures during the wet leakage test after 75 cycles. This indicates that while tape-based solutions may suffice for minor surface damages, they are not suitable for long-term repairs of deep cracks.

5.3 Which repair approach is most suitable for different types of cracks in PV backsheets?

The results of this study indicate that the suitability of a given repair approach heavily depends on the type and severity of the backsheet cracks. For deep, isolated cracks, silicone emerged as the most effective repair material. Its ability to penetrate and completely fill cracks without leaving air gaps, as demonstrated in ATR-IR imaging, makes it particularly suitable for addressing such damage. Furthermore, its elasticity and resistance to shrinkage during curing contributed to its superior performance under accelerated aging conditions.

In contrast, the optimized PU coating was effective in improving the insulation resistance (wet leakage test passed after coating) and filling cracks when applied correctly, but its performance was compromised by cracking after accelerated aging (thermal cycling and damp heat with $-40^{\circ}\text{C} \rightarrow +85^{\circ}\text{C}$ and 85% humidity). The optimized application process and material composition addressed some of these issues, limiting the formation of new cracks to areas directly above the backsheet cracks. However, this approach remains less reliable under severe testing conditions than silicone for deep cracks and is more suited to surface-level or shallow damage where flexibility requirements are lower. When both the crack filler and the topcoat are used, PU coatings can effectively fill both deep and surface cracks. However, if only the topcoat is applied, its higher viscosity limits its ability to fill smaller or narrower cracks, restricting its use to deeper and wider cracks which is why the two layer approach including the crack filler is superior.

Tape-based solutions, such as the 3M PVC foil, are unsuitable for deep cracks due to insufficient adhesive filling capacity. However, they may be viable for small, superficial cracks or as a temporary fix for minor damage. The ease of application for small defects makes tape-based solutions attractive for quick repairs, but application is difficult for full-surface module backsheet repairs. Furthermore, their susceptibility to shrinkage and delamination during aging tests also limits their long-term effectiveness. Tapes should only be used for surface-level microcracks, as their adhesive layer lacks the volume required to fill deeper cracks effectively.

The study also revealed the critical importance of proper preparation and application for all repair approaches. Before applying any repair material, thorough cleaning of the backsheet is essential to remove dust, dirt, and chalking residues that could hinder adhesion. Additionally, care must be taken to ensure that the edges of the backsheet, particularly the border areas near the aluminum frame, are well-covered. This step is vital to maintain electrical insulation and prevent moisture ingress, which could compromise the effectiveness of the repair.

In summary, the silicone coating is the most versatile and effective repair approach for a wide range of crack types, particularly deep and isolated cracks. Its ease of use further enhances their practicality, as they require only a single component and layer for application. Additionally, the absence of solvents in silicone simplifies handling and minimizes potential safety concerns, making them a user-friendly and efficient solution for backsheet repairs.

Polyurethane-based coatings are effective in crack-filling when both crack filler and topcoat are applied, although their application process is more demanding, and their performance under severe testing conditions is less robust. Tape-based solutions are best reserved for localized defects and minor surface-level damage or as a temporary repair option.

5.4 Practical Implications

The findings suggest that repair solutions for PV module backsheets may be more suitable for specific scenarios rather than large-scale applications. In large photovoltaic power plants, replacing modules is often more economical due to the low cost of new modules, especially given the recent price reductions in imported modules from China. However, in small-scale installations, repair methods could offer significant advantages. For example:

- Replacing a single damaged module is often impractical due to differing, lately increased module sizes and incompatibility with existing mounting structures.
- New modules have higher power outputs and therefore may necessitate new inverters and additional labor costs, making repairs more cost-effective.
- Repair solutions are particularly valuable for addressing small backsheet damages caused during transportation or installation.

The development of user-friendly repair kits could make such solutions more accessible, providing a convenient and cost-saving option for minor backsheet repairs.

5.5 Critical Analysis

This study provided valuable insights into the performance of various repair methods. The silicone coating emerged as the most reliable solution, particularly when applied with attention to sealing the frame interface. However, a notable disadvantage of silicone is its inherently "sticky" surface, which tends to attract dirt and remains persistently covered with particles.

The initial problems with the PU coating, including cracking after 25 cycles, were addressed through material and application optimizations, leading to improved performance. Although, the optimized coating was successful in crack-filling and providing a top barrier layer it still failed to withstand the harsh conditions in the accelerated aging tests, suggesting that further improvements are needed. However, it is worth noting that real-world aging observed at the outdoor test site at Bisamberg (Vienna) has not shown any issues with crack formation [16], indicating that the laboratory aging conditions may be significantly more demanding than actual field conditions. It is worth noting that the modules repaired in this study were in significantly worse condition than those repaired at the test site in Bisamberg.

Non-destructive testing methods to check the effectiveness of the repair would be desirable. However, the tests with SAM proved to be only of limited effectiveness in assessing the crack filling, as the spatial resolution of the method is not sufficient and the differences in the sound propagation speed between the polymer of the backsheet and the repair coating are only slight. This underlines the importance of other complementary destructive methods to be able to evaluate the repair methods.

5.6 Limitations

This study was limited to polyamide backsheets with longitudinal cracks, as obtaining modules with different types of backsheet cracks was not feasible. The repair methods tested are a specific repair solution for cracks and are not applicable for defects like backsheet delamination. Further studies are needed to expand the scope and applicability of these repair strategies.

Chapter 6

Summary and Outlook

6.1 Summary

Photovoltaic power generation is poised to become a cornerstone of the upcoming energy transition. Although the manufacturing and deployment of PV modules have risen substantially in recent years, certain reliability issues persist – particularly related to the materials used in module construction. The ReNew PV research project took a leading role in exploring methods to repair damaged backsheets, with special emphasis on polyamide-based backsheets, which are especially prone to cracking. The research project will expand to include other backsheet materials in the future.

This study has explored the investigation and evaluation of repair methods for PV modules with cracked backsheets. By employing a two-phased approach, the study systematically tested repair materials on small samples and full-sized modules under accelerated aging conditions. The results highlight the potential of various coatings and tapes to mitigate backsheet cracks, restore insulation resistance, and prolong module lifespan. While ideal outcomes were not achieved across all tested methods, significant progress was made in refining repair strategies and demonstrating measurable improvements. These findings provide a foundation for further optimization and underline the importance of repair solutions in maintaining the efficiency and safety of PV modules.

6.2 Outlook and Recommendations for Future Work

While the findings highlight the potential benefits of backsheet repair, further research and practical considerations are necessary to fully establish repair as a mainstream solution:

1. **Comparative Studies with Multiple Reference Modules:** Currently, only one reference module was used, and modules showed varying degrees of degradation prior to testing. Future work should include a larger set of modules with identical pre-test degradation levels; this would allow repair coatings to be applied consistently, followed by standardized accelerated aging tests. Such controlled experiments will provide a more definitive understanding of how a repair coating affects electrical performance and whether it offers preventative benefits, such as slowing further performance decline once a crack has formed.
2. **Suitability for Different System Scales and Economic Considerations:** From a sustainability perspective, repair offers a more resource-efficient approach than replacement. Nevertheless, for large-scale PV plants, it may not always be the most cost-effective

solution, especially given the rapid evolution of cell technologies that can make replacing modules more appealing. In contrast, small-scale PV systems, such as residential rooftop installations, often face significant secondary costs – new mounting systems or potential inverter upgrades – when modules are replaced. For these systems, repairing existing modules could be more economical, provided that the module size and electrical parameters remain compatible with existing infrastructure.

3. **Development of a User-Friendly Repair Kit:** One promising direction involves creating a repair kit that could be applied by a homeowner or technician without specialized training, thereby reducing labor costs. By simplifying the repair process and making it accessible to a broader range of users, the overall repair solution can become a low-cost and sustainable alternative to full module replacement in the residential market.
4. **Special Applications in Remote or Difficult-to-Access Locations:** In regions where the transportation of replacement modules is both challenging and expensive – such as remote alpine installations or off-grid systems in hard-to-reach areas – a backsheet repair solution can prove particularly practical. By mitigating or eliminating the high costs of transporting replacement modules, repair becomes an attractive option compared to full module replacement.

In conclusion, the research confirms that backsheet repair can extend the operational life of PV modules and serve as a sustainable alternative to replacement. However, further systematic studies are needed to validate long-term performance gains across a variety of module types and real-world conditions. Economic analyses that account for both large-scale plants and smaller or remote installations will ultimately guide whether repair or replacement is more feasible in each scenario.

By addressing both technical and economic challenges, backsheet repair techniques offer a promising avenue for improving the sustainability and circularity of the photovoltaic industry. As the demand for renewable energy grows, incorporating repair methods alongside preventive measures can help extend the lifespan of PV modules, reduce waste, and contribute to the long-term efficiency of solar energy systems.

Chapter 7

Bibliography

- [1] Agilent Technologies. *Agilent Exoscan 4100 FTIR User Manual*, 2024. Accessed: 2024-07-01.
- [2] Gisele Alves dos Reis Benatto, Claire Mantel, Sergiu Spataru, Adrian Alejo Santamaria Lancia, Nicholas Riedel, Sune Thorsteinsson, Peter Behrendorff Poulsen, Harsh Parikh, Soren Forchhammer, and Dezso Sera. Drone-based daylight electroluminescence imaging of pv modules. *IEEE journal of photovoltaics*, 10(3):872–877, 2020.
- [3] Venkat Aryan, Mercè Font-Brucart, and Daniel Maga. A comparative life cycle assessment of end-of-life treatment pathways for photovoltaic backsheets. *Progress in photovoltaics*, 26(7):443–459, 2018.
- [4] Guy Beaucarne, Gabriele Eder, Emmanuel Jadot, Yuliya Voronko, and Wolfgang Mühleisen. Repair and preventive maintenance of photovoltaic modules with degrading backsheets using flowable silicone sealant. *Progress in photovoltaics*, 30(8):1045–1053, 2022.
- [5] P. Biermayr, S. Aigenbauer, C. Dißauer, M. Eberl, M. Enigl, H. Fechner, C. Fink, M. Fuhrmann, M.-C. Haidacher, F. Hengel, M. Jaksch-Fliegenschnee, K. Leonhartsberger, D. Matschegg, S. Moidl, E. Prem, T. Riegler, S. Savic, C. Strasser, P. Wonisch, and E. Wopienka. Innovative energietechnologien in Österreich 2023: Marktentwicklung 2023. Technical Report 17a/2024, Bundesministerium für Klimaschutz, Umwelt, Energie, Mobilität, Innovation und Technologie (BMK), Wien, Österreich, 2024.
- [6] Claudia Buerhop Lutz, Larry Lüer, Oleksandr Stroyuk, Jens Hauch, and Ian Marius Peters. Dynamics of backsheet-driven insulation issues. *Solar energy materials and solar cells*, 257:112398, 2023.
- [7] Norman B Colthup, Lawrence H Daly, and Stephen E Wiberly. *Introduction to infrared and Raman spectroscopy*. Acad. Pr., Boston, Mass. [u.a.], 3. ed., 2. pr. edition, 1992.
- [8] European Commission. Repowereu with clean energy factsheet, 2022.
- [9] Philipp Danz, Venkat Aryan, Edda Möhle, and Nicole Nowara. Experimental study on fluorine release from photovoltaic backsheet materials containing pvf and pvdf during pyrolysis and incineration in a technical lab-scale reactor at various temperatures. *Toxics (Basel)*, 7(3):47, 2019.
- [10] Wolfgang Demtröder. *Experimentalphysik : 3. Atome, Moleküle und Festkörper*. Springer-Lehrbuch. Springer Spektrum, Berlin Heidelberg, 5., neu bearbeitete und aktualisierte auflage edition, 2016.

- [11] G Eder, Y Voronko, W Mühleisen, C Hirschl, G Oreski, K Knöbl, and H Sonnleitner. Aging induced cracking of polymeric backsheets: Analytical approach to identify the drivers. *IEEE PVSC-46*, 2019.
- [12] G. C. Eder et al. Error analysis of aged modules with cracked polyamide backsheets. *Solar Energy Materials and Solar Cells*, 203:0927–0248, 2019.
- [13] Topic 5.5 Photovoltaics Project Nr.: 867267 Energy Research 4th call. Sustainable photovoltaics, 2018.
- [14] K. P. Bhandari et al. Energy payback time (epbt) and energy return on energy invested (eroi) of solar photovoltaic systems: A systematic review and meta-analysis. *Renewable and Sustainable Energy Reviews*, 47:133–141, 2015.
- [15] Sara Gallardo-Saavedra, Luis Hernández-Callejo, María del Carmen Alonso-García, José Domingo Santos, José Ignacio Morales-Aragón, Víctor Alonso-Gómez, Ángel Moretón-Fernández, Miguel Ángel González-Rebollo, and Oscar Martínez-Sacristán. Non-destructive characterization of solar pv cells defects by means of electroluminescence, infrared thermography, i–v curves and visual tests: Experimental study and comparison. *Energy (Oxford)*, 205:117930, 2020.
- [16] Anika Gassner. *Monitoring of electrical performance and material stability of PV modules with repaired/coated backsheets*. Wien, 2022.
- [17] P. Gebhardt, L. P. Bauermann, and D. Philipp. Backsheet chalking theoretical background and relation to backsheet cracking and insulation failures. 2018. In: *Proceedings of the 35th European Photovoltaic Solar Energy Conference and Exhibition (EU PVSEC)*, 2018.
- [18] Conversio Market & Strategy GmbH. Fluoropolymer waste in europe 2020. Final Report, elaborated for Pro-K, 2022. Accessed: 2025-01-22.
- [19] Martin A. Green. *Solar Cells: Operating Principles, Technology, and System Applications*. Prentice-Hall, 2nd edition edition, 2013.
- [20] Peter R Griffiths and James A De Haseth. *Fourier transform infrared spectrometry*. Chemical analysis 171. Wiley-Interscience, Hoboken, NJ, second edition edition, 2007.
- [21] H. Günzler and H.-U. Gremlich. *IR-Spektroskopie: eine Einführung*. Wiley-VCH GmbH & Co. KGaA, Weinheim, 4th edition, 2003.
- [22] M. Halwachs, L. Neumaier, N. Vollert, L. Maul, S. Dimitriadis, Y. Voronko, G.C. Eder, A. Omazic, W. Mühleisen, Ch Hirschl, M. Schwark, K.A. Berger, and R. Ebner. Statistical evaluation of pv system performance and failure data among different climate zones. *Renewable energy*, 139:1040–1060, 2019.
- [23] Huili Han, Ji Xia, Hongjie Hu, Rensheng Liu, Jiangfeng Liu, Kaushik Roy Choudhury, William J. Gambogi, Thomas Felder, Marisol Rodriguez, Ethan Simon, Zongwen Zhang, and Hui Shen. Aging behavior and degradation of different backsheets used in the field under various climates in china. *Solar Energy Materials and Solar Cells*, 225:111023, 2021.
- [24] H Hu, W Gambogi, KR Choudhury, L Garreau-Iles, T Felder, S MacMaster, O Fu, and TJ Trout. Field analysis and degradation of modules and components in distributed pv applications. In *35th European Photovoltaic Solar Energy Conference and Exhibition*, 2018.
- [25] IEA Photovoltaic Power Systems Programme (IEA-PVPS). Fact sheet update 2023: Pv module reliability. Technical report, International Energy Agency (IEA), 2023. Accessed: 2024-07-01.

- [26] HT Instruments. I-v400w curve tracer datasheet, 2024. Rel. 2.00, Accessed: 2024-10-19.
- [27] International Electrotechnical Commission. *IEC 61215-2: Terrestrial Photovoltaic (PV) Modules – Design Qualification and Type Approval – Part 2: Test Procedures*. IEC, February 2021.
- [28] IRENA and IEA-PVPS. End-of-life management: Solar photovoltaic panels. <https://www.irena.org/publications/2016/Jun/End-of-life-management-Solar-Photovoltaic-Panels>, 2016. Accessed: 2025-01-19.
- [29] D.C. Jordan et al. Compendium of photovoltaic degradation rates. *Progress in Photovoltaics: Research and Applications*, 24(7):978–989, 2016.
- [30] Michael Kempe, Peter Hacke, Joshua Morse, et al. Electrochemical mechanisms of leakage-current in photovoltaic modules. *Progress in Photovoltaics: Research and Applications*, 31(7):700–715, 2023.
- [31] Charles Kittel. *Introduction to Solid State Physics*. Wiley, 8th edition, 2004.
- [32] LibreTexts. Spectroscopy of aromatic compounds. https://chem.libretexts.org/Bookshelves/Organic_Chemistry/Organic_Chemistry_%28OpenStax%29/15%3A_Benzene_and_Aromaticity/15.07%3A_Spectroscopy_of_Aromatic_Compounds, 2024. Accessed: 2024-07-01.
- [33] Sascha Lindig, Julien Deckx, Magnus Herz, Julián Ascencio Vásquez, Marios Theristis, Bert Herteleer, and Kevin Anderson. Best practice guidelines for the use of economic and technical kpis. Technical Report IEA-PVPS T13-28:2024, International Energy Agency Photovoltaic Power Systems Programme (IEA PVPS), December 2024. ISBN 978-3-907281-69-7.
- [34] Roman Gr. Maev. *Acoustic Microscopy*. Wiley-VCH, Weinheim, Germany, 2008.
- [35] Jochen Markert, Sandra Kotterer, Djamel Eddine Mansour, Daniel Philipp, Paul Gebhardt, João M. Serra, and Robert Kenny. Advanced analysis of backsheets failures from 26 power plants. *EPJ Photovoltaics*, 12:7, 2021.
- [36] MB Electronique. *Microscopie Acoustique SAM400: Specifications*, 2024. Accessed: 2024-07-01.
- [37] Laila V. Mesquita, Djamel Eddine Mansour, Paul Gebhardt, and Luciana Pitta Bauermann. Scanning acoustic microscopy analysis of the mechanical properties of polymeric components in photovoltaic modules. *Engineering Reports*, 2(8):e12222, 2020.
- [38] Jacob Millman and Arvin Grabel. *Microelectronics*. McGraw-Hill, 2nd edition, 2009.
- [39] Stefan Mitterhofer, Jan Slapšak, Alexander Astigarraga, David Moser, Guillermo Oviedo Hernandez, Paolo Vincenzo Chiantore, Wei Luo, Yong Sheng Khoo, Jorge Rabanal-Arabach, Edward Fuentealba, Pablo Ferrada, Mauricio Trigo Gonzalez, Julián Ascencio-Vásquez, Marko Topič, and Marko Jankovec. Measurement and simulation of moisture ingress in pv modules in various climates. *IEEE Journal of Photovoltaics*, 14(1):140–148, 2024.
- [40] A. W. Mix and A. J. Giacomini. Standardized polymer durometry. *Journal of Testing and Evaluation*, 39(4):696–705, 07 2011.

- [41] Olympus Corporation. *Olympus SZH Stereo Microscope: Brochure*, 2024. Accessed: 2024-07-01.
- [42] G Oreski, J S Stein, G C Eder, K Berger, L Bruckman, R French, J Vedde, and K A Weiß. Motivation, benefits, and challenges for new photovoltaic material & module developments. *Progress in energy*, 4(3):32003, 2022.
- [43] Michael Owen-Bellini. Duramat may 2020 webinar – backsheet materials for photovoltaic modules. Webinar Presentation, National Renewable Energy Laboratory, 2020. Accessed: 2025-01-22.
- [44] PCE Instruments. *Inspection Camera PCE-MM 800: Data Sheet*, 2024. Accessed: 2024-07-01.
- [45] Vishal E. Puranik, Ravi Kumar, and Rajesh Gupta. Progress in module level quantitative electroluminescence imaging of crystalline silicon pv module: A review. *Solar Energy*, 264:111994, 2023.
- [46] A. E. Pylaev, E. A. Kostikova, A. L. Yurkov, D. I. Kalugin, A. P. Malakho, V. V. Avdeev, V. N. Lepin, L. V. Oktyabr'skaya, and S. V. Minchuk. Velocity and attenuation of acoustic waves in polymers and polymer composites. *Polymer Science, Series D*, 11(3):272–276, 2018.
- [47] Pramod Rajput, Digvijay Singh, K Y Singh, Alagar Karthick, Mohd Asif Shah, Radhey Shyam Meena, and Musaddak Maher Abdul Zahra. A comprehensive review on reliability and degradation of PV modules based on failure modes and effect analysis. *International Journal of Low-Carbon Technologies*, 19:922–937, 04 2024.
- [48] Barbara H Stuart. *Infrared spectroscopy : fundamentals and applications*. Analytical techniques in the sciences. John Wiley & Sons, Chichester, 2004.
- [49] J. Svarc. Solar panel construction, 2020. Accessed: Mar. 2020.
- [50] Thomas L. Szabo and Junru Wu. A model for longitudinal and shear wave propagation in viscoelastic media. *The Journal of the Acoustical Society of America*, 107(5):2437–2446, 05 2000.
- [51] S.M. Sze and Kwok K. Ng. *Physics of Semiconductor Devices*. Wiley, 3rd edition, 2006.
- [52] Tadanori Tanahashi and Takashi Oozeki. Ac impedance characteristics and modeling of electrical leakage circuit within a photovoltaic module installed in a field. *IEEE Journal of Photovoltaics*, 14(3):512–521, 2024.
- [53] J. Tracy et al. Survey of material degradation in globally fielded pv modules. In *2019 IEEE 46th Photovoltaic Specialists Conference (PVSC)*, pages 0874–0879, 2019.
- [54] University of Tartu. Chalk ir spectra (fillers and pigments). Accessed: 2024-12-20.
- [55] Yuliya Voronko, Gabriele Eder, Wolfgang Muehleisen, Lukas Neumaier, Christian Breitwieser, Karl Knöbl, Sonja Feldbacher, Gernot Oreski, and Norbert Lenck. Repair of cracked backsheets: long-term stability. 09 2021.
- [56] Yuliya Voronko, Gabriele Christine Eder, Wolfgang Mühleisen, Lukas Neumaier, Christian Breitwieser, Sonja Feldbacher, Gernot Oreski, Markus Feichtner, and Tudor Dobra. Minimizing crack propagation in cracked pv backsheets through repair coatings. October 2022. Österreichische Fachtagung für Photovoltaik und Stromspeicherung 2022 ; Conference date: 05-10-2022 Through 06-10-2022.

- [57] C. Zhou et al. The methylene infrared vibration and dielectric behavior monitored by amide group arrangement for long chain polyamides. *Polymer*, 190:122231, 2020.

Glossary

1-K	One component
2-K	Two component
AC	Accelerated current
ATR	Attenuated total reflection
CaCO ₃	Calcium carbonate
CCD	Charge-coupled device
CO ²	Carbon dioxid
DC	Direct current
DSTD	Deuterated triglycine sulfate detector
EU	European Union
EVA	Ethylene-vinyl acetate
FT	Fourier-transformation
FTIR	Fourier-transformation infrared
Ge	Germanium
GND	Ground
IR	Infrared
IRHD	International Rubber Hardness Degree
MPP	Maximum Power Point
MQT	Module Quality Test
NIR	Near-infrared
PA	Polyamide
PDMS	Polydimethylsiloxane
PET	Polyethylene terephthalate
PO	Polyolefine
PP	Polypropylen
PU	Polyurethane
PV	Photovoltaics
PVC	Polyvinyl chloride
PVDF	Polyvinylidene difluoride
PVF	Polyvinyl fluoride
RT	Room temperature

Si Silicon
SiC Silicon carbide

TiO₂ Titanium dioxide

UV Ultraviolet

List of Figures

1.1	Overview of PV module structure and defect distribution.	10
1.2	Timeline of backsheet material evolution in photovoltaic modules according to Markus Feichtner, Dr. Gabriele Eder and Dr. Gernot Oreski (personal communication at the PVSEC (European Photovoltaic Solar Energy Conference and Exhibition), September 2024). The nomenclature (e.g., PA/PA/PA) represents multilayer structures, where each material separated by a slash (/) corresponds to a distinct layer in the backsheet composition.	11
2.1	Polyamide backsheet information	15
3.1	Measurement principle of the scanning acoustic microscopy in reflection mode [37]	18
4.1	Overview of the Kyoto 235Wp PV module with cracked BS. The numbers refer to the sample areas where the four repair materials were applied	29
4.2	LM images taken with the handheld USB microscope (left) of one of the sample areas shown in Figure 4.1.	30
4.3	Overview of Coating Processes and Tools	31
4.4	SAM images of the uncoated BS: On the left, the image of the area scan of the surface layer; On the right, the cross sectional scans of the BS.	32
4.5	SAM image of the BS coated with PU: On the left, the image of the area scan of the surface layer; On the right, the cross sectional scans of the BS.	33
4.7	SAM images of the BS coated with silicone (DOWSil): On the left, the image of the area scan of the solar cell layer; On the right, the cross sectional scans of the BS.	33
4.6	SAM image of the BS with tape (3M 1080): On the left, the image of the area scan of the surface layer; On the right, the cross sectional scans of the BS.	34
4.8	Light microscope images of cross-sections of the coated BS.	35
4.9	LM image (top) and ATR-IR image (bottom) of the BS coated with Remisol	35
4.10	Light microscopy image and ATR-IR image of the BS coated with Remisol cover coating without the crack filler. The coating is around 160 μm thick.	35
4.11	Light microscopy image and ATR-IR image of the BS repaired with tape	36
4.12	Light microscopy image and ATR-IR image of the BS coated with silicone	36
4.13	First steps of the silicone coating process	38
4.14	Further steps of the silicone coating process	38
4.15	Application of the crack filler in the Remisol coating process	39
4.16	Application of the cover coating in the Remisol coating process	39
4.17	Application of the 3M PVC foil	40
4.18	Test-setup for wet leakage test	41
4.19	Isolation of the hole in the Remisol coating	41
4.20	Timeline of weathering experiment	42

4.21	Figure with all temperature and humidity steps programmed for one temperature cycle	43
4.22	Comparison of programmed (black for temperature and dark blue for humidity) and measured (red for temperature and light blue for humidity) temperature cycles	43
4.23	Overview of the accelerated aging results for the silicone coating on the backsheet	44
4.24	Artificially aged silicone coating showing few surface near cracks	45
4.25	Light microscopy images of cracked coating after 75 temperature cycles	45
4.26	Overview of the accelerated aging results for the PU coating (Remisol) on Module M2	46
4.27	Artificially aged PU coating showing severe cracking	47
4.28	Overview of the accelerated aging results for the PU cover coating on Module M3	48
4.29	Artificially aged PU coating showing severe cracking	49
4.30	Comparison of the Energy-dispersive X-ray spectroscopy results of the original (left) and the new (right) PU cover coating	49
4.31	The nano-indentation results for the the PU coating before and after 25 TC . . .	50
4.32	Comparison of tensile elongation test results for the original and optimized PU coatings. The diagrams illustrate differences in stress (σ_{\max}) and elongation (ϵ_{\max}) between the two coatings, highlighting the enhanced elasticity (corresponds to higher elongation at break) of the optimized coating.	50
4.33	The original PU coating on Module M7 after 25 TC with the modified application and test parameters	51
4.34	The optimized PU coating on Module M6 after 25 TC with the modified application and test parameters	51
4.35	Overview of the accelerated aging results for the 3M Wrap Tape (The blue spots are color markings and not caused by or linked to degradation)	52
4.36	Ripped Tape after 75 cycles	52
4.37	Overview of the accelerated aging results for the uncoated reference module . . .	53
4.38	Comparison between uncoated reference module before and after 25 temperature cycles	53
4.39	Comparison between uncoated reference module after 50 and 75 temperature cycles	54
4.40	Comparison between IR spectra of the backsheet of the uncoated reference module before and after the 75 temperature cycles	54
4.41	Comparison of the IR spectra of the silicone coating before and after the 75 temperature cycles	55
4.42	The IR spectra of chalk from [54]	56
4.43	Comparison between the IR spectra of the 3M PVC Foil before and after the 75 temperature cycles	57
4.44	Comparison of the IR spectra of the Remisol coating before and after 50 temperature cycles	58
4.45	Comparison of the IR spectra of the original and the optimized PU cover coating (before the accelerated aging test)	59
4.46	Comparison of the IR spectra of the optimized PU cover coating before and after 25 temperature cycles	59
4.47	Calculated P_{\max} for standard conditions before and after the temperature cycles and the power degradation in percent. The modules are rated for a peak power of 240 W	60
4.48	Comparison of EL images of modules M1–M5 before and after the 75 TC aging process.	63

List of Tables

2.1	Comparison of the electrical characteristics (power P_{MPP} , voltage U_{MPP} and current I_{MPP} at the maximum power point; open-circuit voltage U_{OC} and short-circuit current I_{SC}) of the modules according to the type label of Module 1-5 (240Wp), Module 6 (210Wp) and Module 7 (235Wp) specifications.	16
3.1	Key Parameters of the I-V-400w from HT Instruments	23
4.1	Overview of repair materials (Abbreviations: RT: Room Temperature; 1-K: 1 component system; 2-K: 2 components system).	28
4.2	Overview of Repair Methods and Materials	37
4.3	Insulation Resistance (R_{iso}) of coated Modules from the Wet Leakage Test	40
4.4	P_{max} comparison before and after the accelerated aging test.	60